NAVAL ARCHITECTURE AND MARINE ENGINEERING

UNIVERSITY of MICHIGAN ■ COLLEGE of ENGINEERING

Evaluation of Advanced Turbulence Models for High-Reynolds Number External Flow

Grzegorz Filip, Kevin Maki

The University of Michigan
Department of Naval Architecture & Marine Engineering
Ann Arbor, Michigan, USA
gfilip@umich.edu, kjmaki@umich.edu

Technical Report Number 354

January 20, 2015

Abstract

In this report several modern turbulence modeling techniques with applications to high-Reynolds number external flow are critically evaluated. Fully developed turbulent channel flow and the flow past the Ahmed body with a slant angle of 25° are both used to benchmark several LES and DES models for turbulence closure. Channel flow is simulated at two different Reynolds numbers and both the LES and DES approaches are found to exhibit predictive capabilities but with several limitations, especially at the higher Reynolds number. The flow past the Ahmed body is validated against several experimental measurements. The improved delayed detached eddy-simulation (IDDES) model is found to yield the best overall drag prediction, but the wall-modeled LES approach is more robust across a wide range of grid resolutions. The computational effort required to perform the Ahmed-body simulations is summarized together with recommendations for the future use of the turbulence modeling techniques that are evaluated herein.

Keywords: Aerodynamics, Hydrodynamics, CFD, LES, DES, turbulence modeling

1 Introduction

Numerical simulation of complex external flows is an important component of many industrial projects such as automotive and aircraft design, wind turbine modeling, top-side load prediction, and building physics. In many fields, wind tunnel testing is still widely used but the need for reliable numerical tools is growing due to the relatively low cost associated with computer simulations and many additional benefits that they provide. Some of the key benefits include automated optimization through adjoint methods and reduced design evaluation time through massively parallel simulations.

One of the major challenges in industrial application of computational fluid dynamics (CFD) tools is the need to robustly and accurately simulate challenging and important flow physics. High-Reynolds number external flows typically exhibit complex separation and reattachment phenomena in regions of adverse pressure gradients. The CFD method employed to simulate this type of a flow must successfully predict each stage of the flow with little or no external input from the designer. As the field of numerical simulation matures, new improved methods with a higher degree of accuracy and robustness are developed and applied to practical industrial problems. For example, relatively inexpensive but limited Reynolds-Averaged Navier-Stokes (RANS) methods are being superseded in aerodynamic applications by large-eddy simulations (LES) and hybrid methods such as detached-eddy simulations (DES) that combine RANS and LES. These methods are significantly more computationally expensive but they become enabled by the availability of larger and faster computational clusters. It is important to benchmark and validate new methods to ensure their effectiveness and benefit in industrial applications.

The aim of this report is to summarize two important turbulent-flow benchmarking studies that employ several modern LES and DES techniques. The first case is the canonical flow of the fully-developed turbulent channel flow at two Reynolds numbers. Channel flow involves a fully attached turbulent boundary layer and a bulk flow driven by a pressure gradient between two parallel no-slip walls. The simple geometry of this case facilities inexpensive simulations where the viscous sublayer can be fully resolved or modeled. The second benchmark is the flow past a simplified ground vehicle originated by Ahmed et al. [1]. This external aerodynamic flow contains many of the flow features found in real ground vehicle flows such as the transition from laminar to turbulent flow, attached turbulent boundary layers, as well as geometry and pressure gradient induced flow separation. The complex separated flow in the wake of the vehicle has been studied extensively both using physical experiments and numerical simulations because of this prevalent and nonlinear flow feature has significant implications on the vehicle drag and fuel consumption.

The report is organized as follows. The numerical method and the turbulence modeling techniques are described first. Then results for the channel flow problem

are presented and discussed with respect to the simulation results from published direct numerical simulations (DNS). Next the Ahmed body case is described and results of the identification of salient flow features, near-body flow characteristics, and the contributions to the aerodynamic drag are discussed. The computational effort required to perform the Ahmed body simulations is also summarized before the concluding remarks are presented.

2 Numerical Method

Variants of two main turbulence modeling methodologies in the form of large-eddy simulations and detached-eddy simulations are evaluated in this work. Both methods are based on spatially-filtered governing equations of the flow [6]. In large-eddy simulation, a spatial filtering procedure separates the large resolved scales from the so-called subgrid scales. Unlike in RANS methods, the aim of LES is to resolve a large portion of the turbulent spectrum in space and time and to model only the smallest scales. The filter is formally applied to the governing equations of the flow or the Navier-Stokes equations to yield:

$$\frac{\partial \overline{u}_i}{\partial x_i} = 0, \tag{2.1}$$

$$\frac{\partial \overline{u}_i}{\partial t} + \frac{\partial \overline{u}_i \overline{u}_j}{\partial x_j} = -\frac{1}{\rho}\frac{\partial \overline{p}}{\partial x_i} + \frac{\partial}{\partial x_j}\left(\nu\left(\frac{\partial \overline{u}_i}{\partial x_j} + \frac{\partial \overline{u}_j}{\partial x_i}\right) - \tau_{ij}\right) \tag{2.2}$$

presenting the filtered incompressible continuity and momentum equations where the over-bar represents a filter quantity. In many practical applications of LES, an implicit filter associated with the grid and the discretization schemes is assumed and no formal filtering is performed [11]. The implicit filter is assumed in this work and the explicit filtering procedure is only used to dynamically compute the coefficients of the dynamic LES models. The influence of the modeled subgrid scales on the resolved scales is included through the subgrid-scale (SGS) stress τ_{ij} that appears in the filtered momentum equations. The SGS stress is defined as $\tau_{ij} = \overline{u_i u_j} - \overline{u}_i \overline{u}_j$ and can be modeled with a wide range of methodologies ranging from the functional eddy-viscosity type to the structural scale-similarity type.

Hybrid LES/RANS methods are designed to behave like LES in sufficiently resolved regions of the flow and like RANS in the proximity of walls where the turbulent structures become small and thus difficult to resolve fully in space and time [22]. The RANS methods are extensively validated for a range of attached boundary layer flows and their use in the near-wall region can greatly reduce the grid size requirements for DES compared to pure LES.

All results are computed using OpenFOAM version 2.3.

2.1 Turbulence Modeling

In this work, large-eddy simulations are performed using the one-equation eddy-viscosity (OEE) model of Yoshizawa and Horiuti [29] and its dynamic variant (DOEE) from Kim and Menon [15]. The dynamic model attempts to automatically adjust to the resolved flow features through an explicit grid filtering to compute local coefficients for its transport equation. The most recent one-equation DES model of Shur et al. [21] in the form of the improved delayed detached-eddy simulations (SA-IDDES) is also evaluated.

2.1.1 One-Equation Eddy-Viscosity Models

The one-equation eddy-viscosity model is based on Yoshizawa and Horiuti [29] and Kim and Menon [15], and a brief overview is given here to allow for comparison between the different approaches.

Transport-equation based LES models are designed to improve the subgrid modeling by including non-local and memory effects of the subgrid terms that are typically not incorporated into algebraic-type models. The one-equation model used here relates the turbulent viscosity ν_{sgs} to the subgrid-scale turbulent kinetic energy k_{sgs} by:

$$\nu_{\text{sgs}} = C_k \overline{\Delta} k_{\text{sgs}}^{1/2} \tag{2.3}$$

that is transported using:

$$\frac{\partial k_{\text{sgs}}}{\partial t} + \frac{\partial \overline{u}_j k_{\text{sgs}}}{\partial x_j} = -\tau_{ij}\frac{\partial \overline{u}_i}{\partial x_j} - C_\varepsilon \frac{k_{\text{sgs}}^{3/2}}{\overline{\Delta}} + \frac{\partial}{\partial x_j}\left(\nu_{\text{sgs}}\frac{\partial k_{\text{sgs}}}{\partial x_j}\right). \tag{2.4}$$

The first term on the right-hand side is the production term and the second term is the dissipation term. The coefficients C_ε and C_k are determined as constants from canonical flow studies or computed dynamically as a function of space and time in the dynamic variant of the one-equation model. The subgrid-scale stress is then modeled as:

$$\tau_{ij} = -2\nu_{\text{sgs}}\overline{S}_{ij} + \frac{1}{3}\delta_{ij}\tau_{kk} \tag{2.5}$$

where $\overline{S}_{ij}$ is the resolved strain rate tensor.

The dynamic procedure of Germano et al. [7] is applied to formulate the dynamic version of the one-equation model. A larger test filter $\widehat{\Delta}$ is used to determine the model coefficients by relating the resolved stresses within the test window T_{ij} to the subgrid-scale stresses:

$$L_{ij} = T_{ij} - \tau_{ij} = \widehat{\overline{u}_i\overline{u}_j} - \widehat{\overline{u}}_i\widehat{\overline{u}}_j. \tag{2.6}$$

The subtest-scale stress is modeled in the same manner as the subgrid-scale stress:

$$T_{ij} = -2\nu_{\text{sgs}}\widehat{\overline{S}}_{ij} + \frac{1}{3}\delta_{ij}T_{kk} \tag{2.7}$$

to yield an equation for the coefficient C_k:

$$L_{ij} - \frac{1}{3}\delta_{ij}L_{kk} = 2C_k M_{ij} \tag{2.8}$$

where

$$M_{ij} = -\widehat{\Delta}K^{1/2}\widehat{\overline{S}}_{ij} + \widehat{\overline{\Delta}k_{\text{sgs}}^{1/2}\overline{S}_{ij}} \tag{2.9}$$

and $K = L_{ii}/2 + \widehat{k}_{\text{sgs}}$ is obtained from the test filtering procedure. The least-squares method is used to solve:

$$C_k = \frac{1}{2}\frac{L_{ij}M_{ij}}{M_{ij}M_{ij}} \tag{2.10}$$

The dissipation rate coefficient C_ε is obtained from relating the test level E and the grid level ε dissipation rates in a similar manner as the turbulent kinetic energy:

$$F = E - \widehat{\varepsilon} = \nu\left(\widehat{\frac{\partial\overline{u}_i}{\partial x_j}\frac{\partial\overline{u}_i}{\partial x_j}} - \frac{\partial\widehat{\overline{u}}_i}{\partial x_j}\frac{\partial\widehat{\overline{u}}_i}{\partial x_j}\right). \tag{2.11}$$

The coefficient is then calculated directly from:

$$F = C_\varepsilon\left(\frac{K^{3/2}}{\widehat{\Delta}} - \widehat{\frac{k_{\text{sgs}}^{3/2}}{\overline{\Delta}}}\right). \tag{2.12}$$

The phenomena of energy backscatter can be approximated through the one-equation formulation unlike in the case of the original Smagorinsky model where the transfer of energy from the smallest scales to the larger turbulent scales typically results in numerical instability. The formulation of the one-equation model ensures a balance of the subgrid turbulent kinetic energy and thus an automatic limiting mechanism that prevents this type of numerical instability [4].

2.1.2 Improved Delayed Detached-Eddy Simulations Model

The detached-eddy simulation methodology is a hybridization of RANS and LES methods with the ultimate goal of improved accuracy and robustness in industrial applications. Originally proposed by Spalart et al. [24], DES is based on a modification of the Spalart-Allmaras RANS turbulent model to dynamically determine the local turbulent length scale and to switch between RANS modeling in attached boundary layers and to LES in regions of separated flow. In practical applications of the original DES model, grid refinement can result in under-prediction of the wall-stresses or modeled stress depletion (MSD) due to a premature switch from RANS to LES based on the computed length scale. Grid-induced separation (GIS) can be a by-product of this phenomena [22]. Delayed detached-eddy simulation (DDES) was formulated to avoid MSD in ambiguously-refined grids through the

introduction of a shielding function that incorporates the eddy viscosity in determining when to switch between the RANS and LES regions.

A further extension of the DDES concept is the improved delayed detached-eddy simulation (IDDES) proposed by Shur et al. [21]. The objective of IDDES is to combine the benefits of wall-modeled LES (WMLES) and DDES for industrial applications with complex geometry and ambiguous grid refinements. Through shielding functions and solution-based parameters, the model switches between WMLES (when turbulent inflow is prescribed) and DDES otherwise.

Unlike in the original DES formulation, in IDDES the subgrid length-scale Δ is a piecewise function incorporating wall-distance dependency and local cell size information:

$$\Delta = \min\{\max\left[C_w d_w, C_w h_{max}, h_{wn}\right], h_{max}\} \tag{2.13}$$

where C_w is a constant computed from simulations of the turbulent channel flow, d_w is the distance to the wall, h_{max} is the maximum edge-length of a cell, and h_{wn} is the wall-normal grid spacing. The modified subgrid length-scale accounts for the effects of anisotropic grids that are commonly used in industrial simulations with complex geometry. The formulation results in a significant variation of the length-scale in the flow and thus often leading to helpful flow destabilization.

The DDES branch of IDDES is designed to activate in flows without turbulent inflow content and more importantly in cases where the grid is unlikely to resolve the dominate energy-carrying eddies. The model length-scale used in the production term of the $\tilde{\nu}$ transport equation is defined as:

$$l_{\text{DDES}} = l_{\text{RANS}} - f_d \max\{0, (l_{\text{RANS}} - l_{\text{LES}})\} \tag{2.14}$$

where l_{RANS} is the original length-scale of the Spalart-Allmaras (SA) model and the delaying function f_d is solution-based through:

$$f_d = 1 - \tanh\left[(8r_d)^3\right] \tag{2.15}$$

where r_d is calculated as in the original SA model [23]. The LES length-scale l_{LES} is a function of the subgrid length-scale through:

$$l_{\text{LES}} = C_{\text{DES}} \Psi \Delta \tag{2.16}$$

where Ψ is a low-Reynolds number correction function to counteract the activation of the original SA RANS model in the LES regime [22].

The wall-modeled large-eddy simulations (WMLES) branch of IDDES is activated when unsteady turbulent inflow is provided and when the grid can sufficiently resolve the dominant eddies in the boundary layer [28]. The WMLES length-scale is computed as:

$$l_{\text{WMLES}} = f_B(1 + f_e) l_{\text{RANS}} + (1 - f_B) l_{\text{LES}} \tag{2.17}$$

where two functions f_B and f_e control the interaction between LES and RANS models. The blending function f_B is designed to improve the switching behaviour

between LES and RANS based on the distanced to the wall and the local maximum cell edge length:

$$f_B = \min\{2\exp(-9\alpha^2), 1.0\} \tag{2.18}$$

where $\alpha = 0.25 - d_w/h_{\max}$. The f_e function acts to prevent the log-layer mismatch that can manifest in DES and DDES simulations:

$$f_e = \max\{(f_{e1} - 1), 0\}\Psi f_{e2}. \tag{2.19}$$

The f_{e1} term is a function of α and thus it is grid dependant only whereas f_{e2} is a function of the solution by incorporating the term $\Sigma_{ij}\left(\partial u_i/\partial x_j\right)^2$. A detailed description of the IDDES formulation can be found in Shur et al. [21].

3 Turbulent Channel Flow

The canonical problem of the fully-developed turbulent channel flow is studied using several forms of turbulence modeling relevant to high-Reynolds number external flow simulations. The problem consists of flow between two parallel plates. The streamwise and spanwise boundaries are typically simulated as cyclic or periodic boundaries to yield plates that are effectively of infinite span. This well-studied flow is an attractive benchmark for CFD solvers and turbulence models because of the availability of the direct numerical simulation (DNS) data and because of the relative simplicity of the problem setup. The DNS data has been used extensively for the evaluation of new turbulence models because a modeling approach that cannot sufficiently resolve the main flow features of the channel flow is unlikely to perform well in aerodynamic applications involving complex geometries and a wide range of turbulent flow structures.

Channel flow simulations performed here are benchmarked against the DNS data at two Reynolds number: $Re_\tau = 395$ from Kim et al. [14] and $Re_\tau = 4,200$ from Lozano-Durán and Jiménez [17]. The Reynolds number is based on the shear velocity u_τ and the half height of the channel δ:

$$Re_\tau = \frac{u_\tau \delta}{\nu} \tag{3.1}$$

where the shear velocity is defined as $u_\tau = \sqrt{\tau_w/\rho}$ with τ_w as the wall shear stress. The fluid is described by its kinematic viscosity ν and density ρ. The lower Reynolds number facilitates relatively inexpensive wall-resolved large-eddy simulations that can be evaluated against hybrid RANS/LES models. The higher Reynolds number flow at $Re_\tau = 4,200$ or $Re_\delta = 1.3 \times 10^5$ is relevant to full-scale external flows such the external aerodynamics of a vehicle where typical body-length-based Reynolds number is on the order of at least $O(10^6)$.

Re_τ	N_y	Turb. Model	Average y^+	Wall Treatment	$\Delta t U/\delta$ (-)
395	96	DOEE	0.9	Resolved	0.007
395	96	DOEE	0.9	Modeled	0.007
395	96	SA-IDDES	0.9	Resolved	0.012
395	96	SA-IDDES	0.9	Modeled	0.010
395	25	DOEE	10	Modeled	0.019
395	25	SA-IDDES	10	Modeled	0.017
4,200	96	DOEE	10	Modeled	0.013
4,200	96	SA-IDDES	12	Modeled	0.011
4,200	25	DOEE	60	Modeled	0.020
4,200	25	SA-IDDES	170	Modeled	0.023
4,200	52	SA-IDDES	80	Modeled	0.021
4,200	138	SA-IDDES	30	Modeled	0.016

Table 3.1: Summary of the fully-developed turbulence channel flow simulations

The wall-modeled LES is benchmarked against the DES approach using this case because fully resolving the viscous sublayer at such Reynolds numbers becomes prohibitive in an industrial setting. The simulations are performed on fully hexahedral grids and using second-order temporal and spatial discretization schemes. The time-step size is automatically adjusted at run-time to limit the maximum Courant number to 0.5. The flow statistics are collected using data over the time window of 200 dimensionless flow-overs.

The configuration of the computational domain is adapted from previous DNS and LES simulations of fully-developed turbulent channel flow. The coordinate system is orientated with positive x in the direction of the mean flow, y is the wall-normal direction, and z is the spanwise direction. The computational domain is $L_x = 2\delta\pi$ long and $L_z = \delta\pi$ wide. The length and width of the domain is discretized with 96 cells in all cases and the number of cells in the wall-normal direction N_y is varied as summarized in Table 3.1. The variation in the wall-normal resolution is used to study the influence of the near-wall treatment on the main features of the flow. Furthermore, the wide range of dimensionless distance to the wall (y^+) is used to evaluate the flexibility of the universal-wall function described by Spalding [25]. The flow is driven by a pressure gradient that is computed at run-time based on a desired bulk velocity. The bulk velocity is modified between the two Reynolds number cases to obtain the appropriate shear velocity and thus the correct shear-velocity-based Reynolds number.

3.1 Velocity Profiles

The important turbulent channel flow results that are studied herein include the mean streamwise velocity and the RMS velocity components (normalized by the

shear velocity). The mean quantity must be predicted accurately to successfully describe the bulk flow within the channel. The resolution of the fluctuating or the RMS components is important in predicting the turbulent length-scales responsible for the turbulent energy cascade [18]. Furthermore, the fluctuating velocity components must be sufficiently resolved in order to simulate phenomena such as noise generation, turbulent diffusion, and complex flow interaction in the wake of bluff bodies.

3.1.1 Channel flow at $Re_\tau = 395$

The dynamic one-equation model (DOEE) and the improved delayed detached-eddy simulation (IDDES) approach are first applied to the channel flow problem at $Re_\tau = 395$ with a fully-resolved viscous sublayer where the first point off the channel walls is placed to give the maximum y^+ of less than one with $N_y = 96$. The mean and RMS velocity quantities are summarized in Figure 3.1. Both turbulence modeling methodologies successfully predict the mean streamwise velocity component throughout the viscous sublayer and the buffer region below $y^+ \approx 30$. The solution is slightly over predicted in the log-law region beyond the buffer. This small deviation from the reference DNS data can be related to the somewhat under predicted RMS velocity components in the same region. The grid used for this test case utilities cell-stretching and thus the cells near the middle of the channel are much larger than those found close to the wall. The larger cells result in a coarser local refinement that may lead to the reduced resolution of the fluctuating components. Close to the wall, the RMS quantities closely match the reference data using both DOEE and IDDES. The peak of the streamwise component is slightly over predicted but the overall trends of the RMS quantities are well captured by both turbulent modeling approaches.

The IDDES model switches between RANS and LES modes approximately five cells away from the wall ($y^+ \approx 5$) without inducing the log-layer mismatch. Figure 3.2 illustrates the RANS region in blue and the LES region in red together with overlaid velocity vectors near one of the channel walls. The attached boundary layer is modeled by the RANS model and approximately 97% of the flow is fully resolved with LES.

The same wall-resolved grid is also simulated with the Spalding wall function to ensure that the resolution of the boundary layer and its effect on the bulk flow are unaffected by employing the universal-wall model. The wall-function results are shown in Figure 3.3. The mean streamwise velocity as well as the RMS velocity components are unaffected by the introduction of the wall function. The same profiles are obtained in the wall-modeled and the wall-resolved simulations and thus the wall function is found to be sufficiently robust on the wall-resolved grid ($y^+ \approx 1$).

The robustness of the wall function is examined at this relatively low Reynolds number by generating a coarser grid in the wall-normal direction where the first

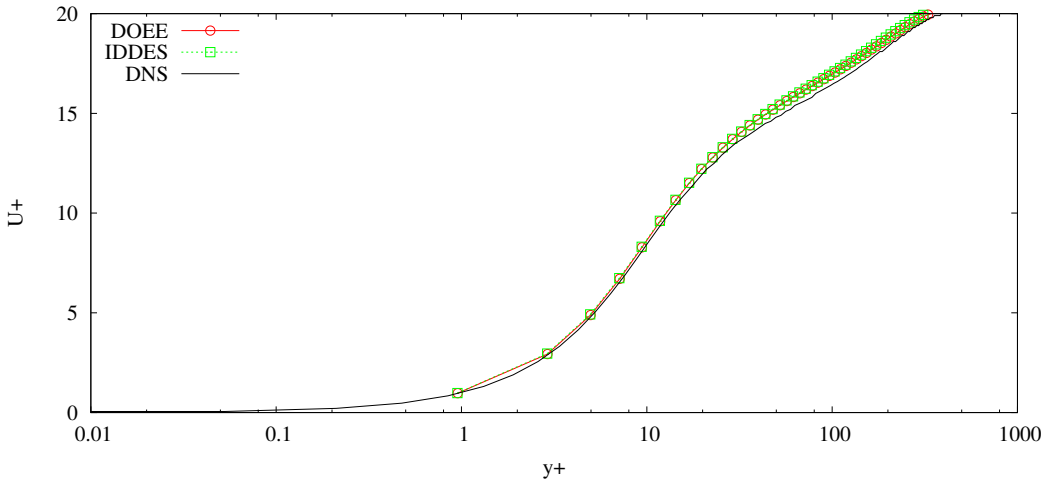

(a) Mean streamwise velocity

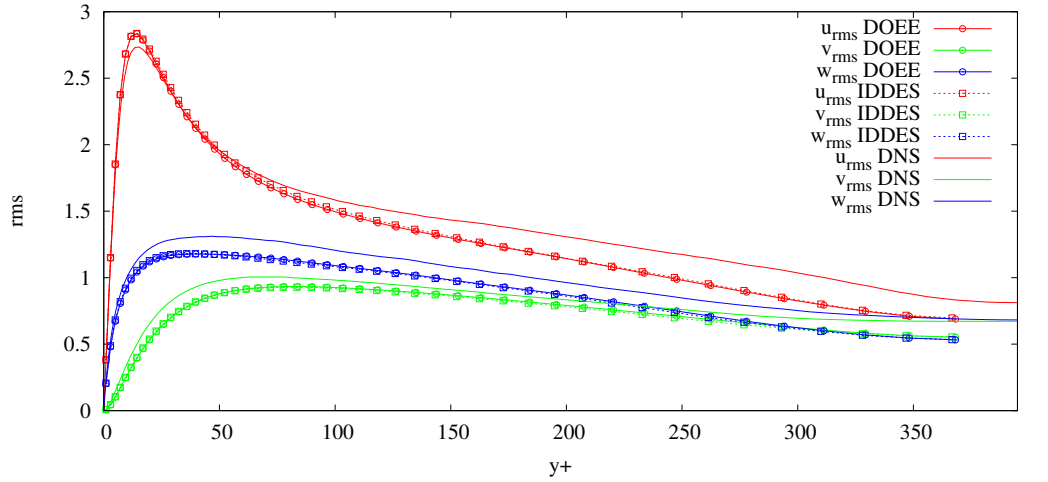

(b) RMS velocity components

Figure 3.1: Channel flow at Re_τ=395 with $y^+ = 0.9$ and no wall function

cell off the wall is located at $y^+ \approx 10$. The coarse grid consists of 25 uniformly-spaced cells in the wall-normal direction and approximately 220,000 total cells. This wall-function grid contains 75% fewer cells relative to the wall-resolved grid. The near-wall spacing selected for this grid is dictated by the maximum wall-normal spacing on the wall-resolved grid in the center of the domain. By matching the largest cell sizes between the two grids, the spatial resolution of the bulk flow is mostly unaffected in the center of the domain. However, the resultant average y^+ of approximately 10 places the first cell off the wall in the buffer region where the universal wall function is expected to preform poorly especially at the low Reynolds number [3].

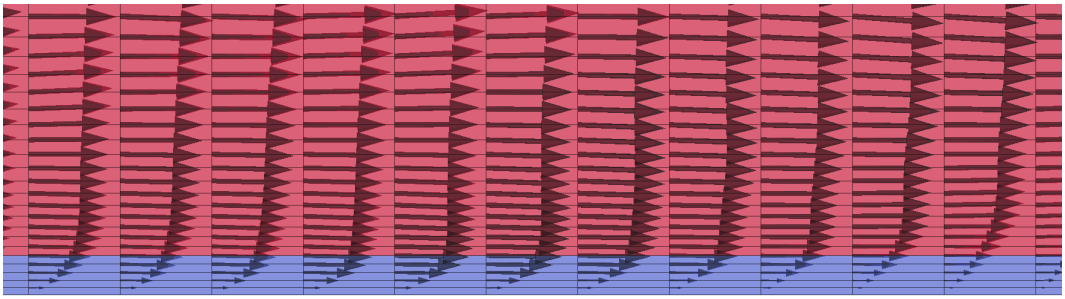

Figure 3.2: Near-wall velocity vectors and the RANS (blue) and LES (red) regions for the wall-resolved IDDES simulation at $Re_\tau = 395$

The wall-modeled results for $Re_\tau = 395$ are shown in Figure 3.4. The near-wall $U+$ prediction matches the DNS reference data but the log layer profile is over predicted with both DOEE and IDDES. Furthermore, the location of the streamwise RMS velocity peak is offset towards the center of the domain due to the insufficient resolution near the buffer region but the spanwise and wall-normal components are relatively close to the DNS data even with an extremely coarse wall-normal resolution.

3.1.2 Channel flow at $Re_\tau = 4,200$

The wall function is examined further by simulating the turbulent channel flow at a larger Reynolds number of $Re_\tau = 4,200$ or the channel half-width based Reynolds number of $Re_\delta = 1.3 \times 10^5$. The larger Reynolds number is more relevant to full-scale automative-aerodynamic or marine-hydrodynamic flows where the turbulence modeling techniques and computational-cost effective wall treatments are critical to render numerical tools feasible for industrial design and engineering use.

The same grid from the lower Reynolds number case with $N_y = 96$ and cell stretching yields an average y^+ of approximately 10 at the higher Reynolds number. The velocity profiles computed for this case are shown in Figure 3.5. The wall-modeled LES with the dynamic one-equation model largely over predicts the majority of the mean streamwise velocity component whereas the IDDES simulation successfully predicts the velocity profile. The blending and RANS-boosting functions built into the IDDES formulation successfully alleviate the issue of log-layer mismatch. The DOEE results indicate that the model is not dissipating enough energy in the near-wall region and thus the bulk flow results are overestimated. The results of the fluctuating velocity components also show much larger peak streamwise and spanwise components for the DOEE simulation relative to the DNS data. The magnitude of the peaks resulting from the IDDES simulation are closer to the DNS results but the location of the peaks are again

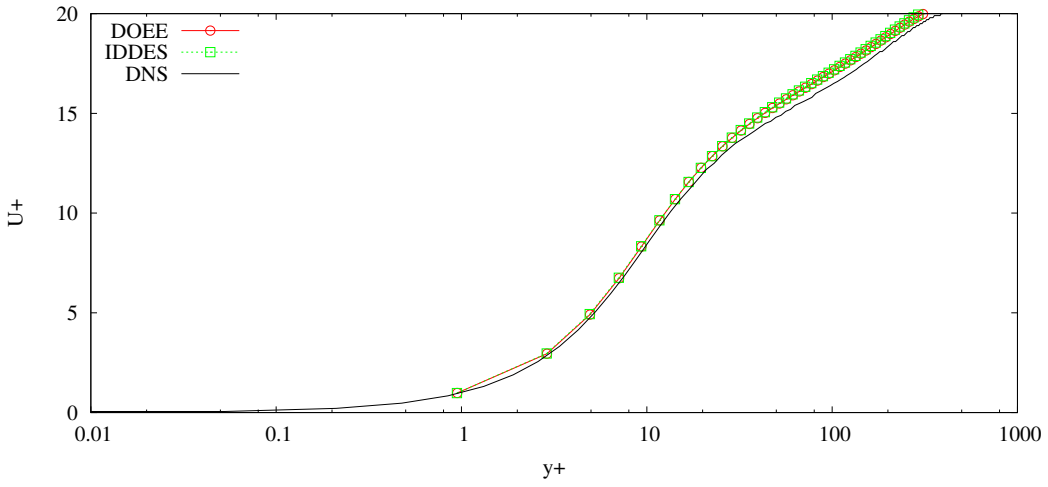

(a) Mean streamwise velocity

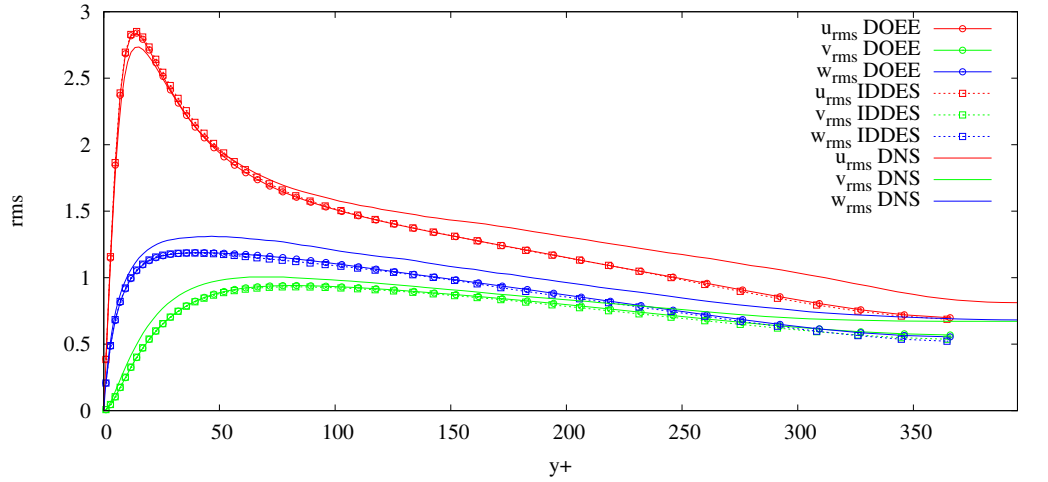

(b) RMS velocity components

Figure 3.3: Channel flow at Re_τ=395 with $y^+ = 0.9$ and with a wall function

offset towards the center of the domain and away from the walls.

The coarser grid with $N_z = 25$ and uniform spacing is simulated at the higher Reynolds number to investigate the sensitivity of the wall function to the near-wall spacing. With DOEE, the coarser grid results in an average y^+ of approximately 60 whereas with IDDES, the average y^+ is approximately 170. The velocity profiles are summarized in Figure 3.6. Similar to the $N_z = 96$ grid, the DOEE simulation over predicts the mean streamwise velocity component. The wall-modeled DOEE simulation is unable to dissipate sufficient energy from the bulk flow even with the dynamic calculation of the model coefficients based on the resolved flow. The relatively coarse resolution within the bulk of the flow is expected to de-

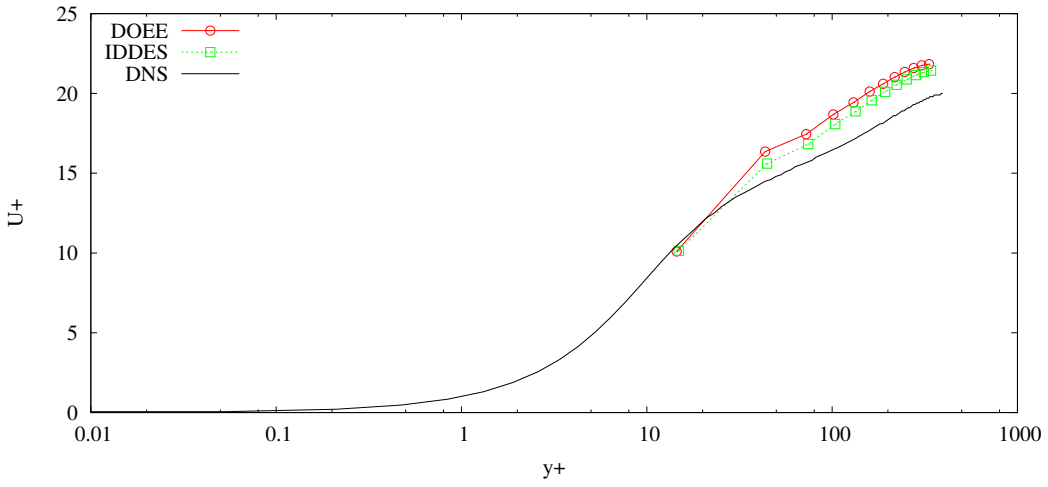

(a) Mean streamwise velocity

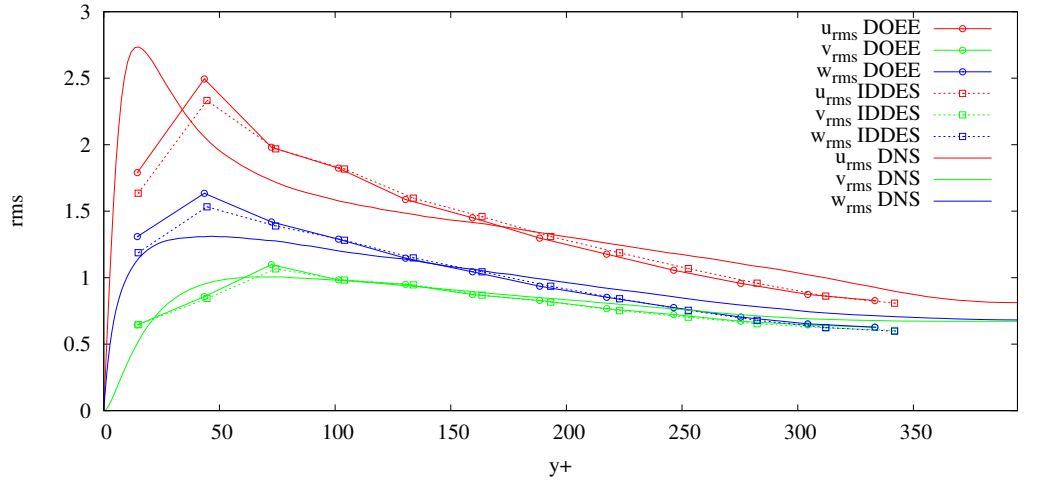

(b) RMS velocity components

Figure 3.4: Channel flow at Re_τ=395 with $y^+ = 10$ and with a wall function

grade the performance of the dynamic procedure because the content used by the procedure is under-resolved and thus the resultant model coefficients do not accurately describe the subgrid-scale behaviour. The IDDES model relies on the RANS mode together with the universal wall function to model the thin attached boundary layer and to successfully predict the mean streamwise velocity profile. However, the RMS quantities in the range of $y^+ \approx 1500$ are under predicted and the near-wall peak magnitude is not resolved. This is because the RANS region includes the first two to three cells off the walls and it is active in approximately 18% of domain. The DOEE model results are somewhat better in terms of peak magnitude but the location of the peaks is offset by approximately 500 wall units

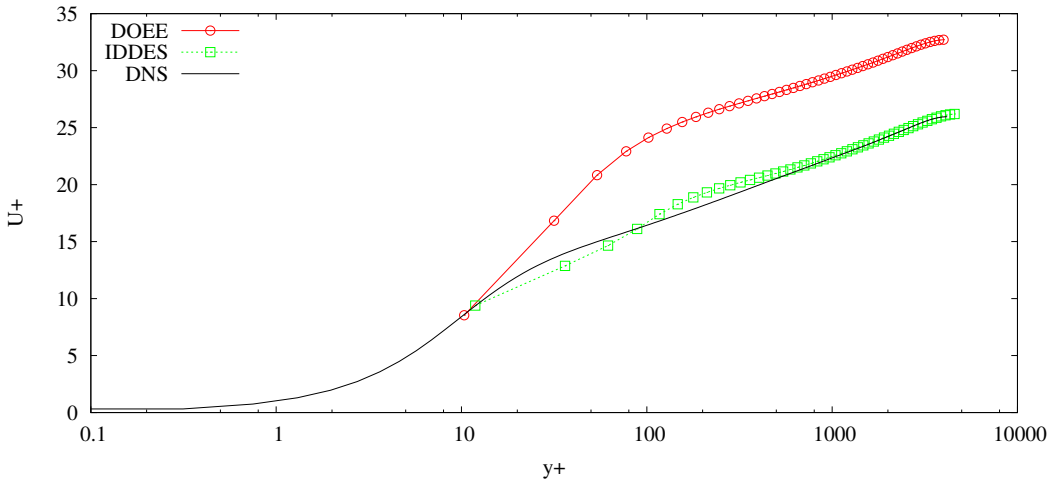

(a) Mean streamwise velocity

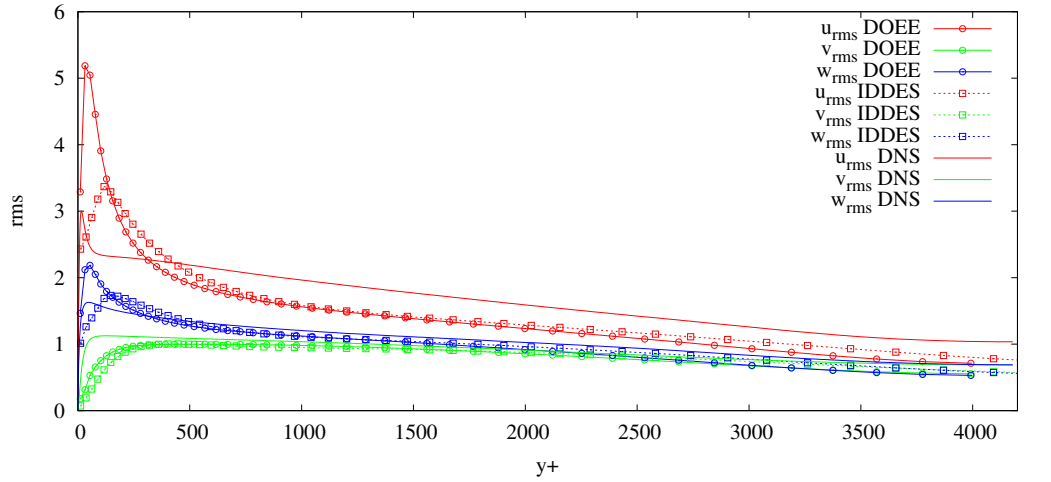

(b) RMS velocity components

Figure 3.5: Channel flow at Re_τ=4,200 on the $N_z = 96$ grid with $y^+ = 10$ and with a wall function

towards the middle of the channel. Nonetheless, the DOEE results are better in predicting the energetic near-wall behaviour compared to the IDDES results that heavily dampen the near-wall fluctuations. The strong damping of the near-wall fluctuations are related to the blending and shielding functions acting too conservatively and enforcing the RANS mode and delaying the activation of the LES mode.

The sensitivity of the IDDES model to the near-wall resolution and its ability to predict the near-wall fluctuations are studied by varying the average y^+ on a series of four grids. Two additional grids are evaluated and the results are sum-

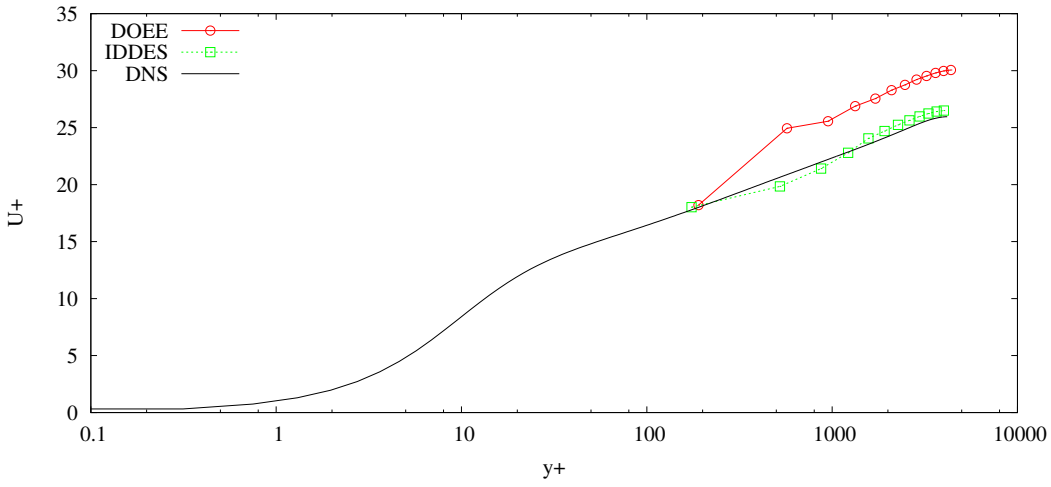

(a) Mean streamwise velocity

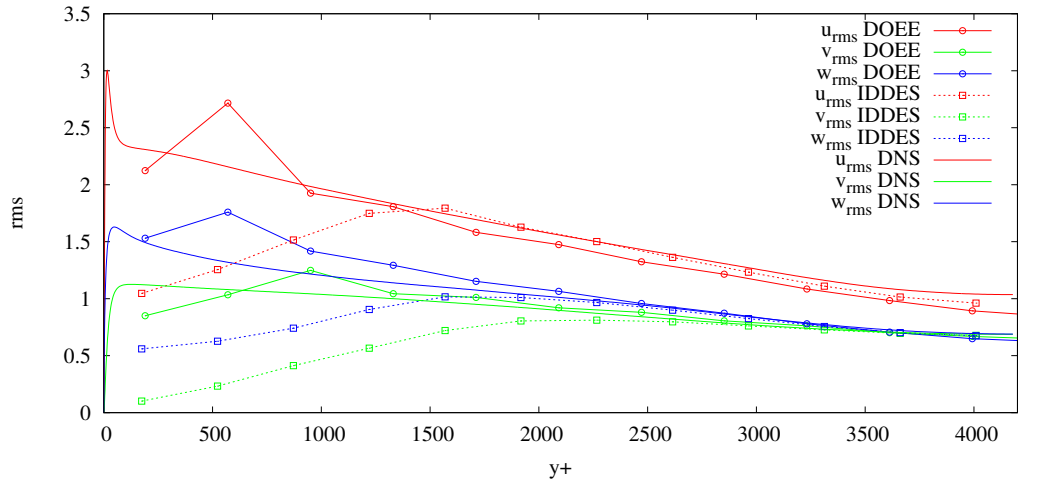

(b) RMS velocity components

Figure 3.6: Channel flow at Re_τ=4,200 on the $N_z = 25$ grid with a wall function

marized in Figures 3.7 and 3.8. The finest ($y^+ \approx 10$) and the coarsest ($y^+ \approx 170$) results are supplemented with a $y^+ \approx 30$ grid where the first grid point is located near the end of the buffer region and a $y^+ \approx 80$ grid. The mean $U+$ results show that placing the first grid point towards the end of the buffer region can adversely affect the prediction of the entire streamwise velocity profile. Additionally, the finest grid with the first grid point placed in the middle of the buffer region under predicts the profile between approximately $20 \leq y^+ \leq 50$ and over predicts the profile between approximately $120 \leq y^+ \leq 500$.

The RMS velocity components are compared in Figure 3.8. Finer grids are more capable of resolving the near-wall fluctuations due to a larger portion of

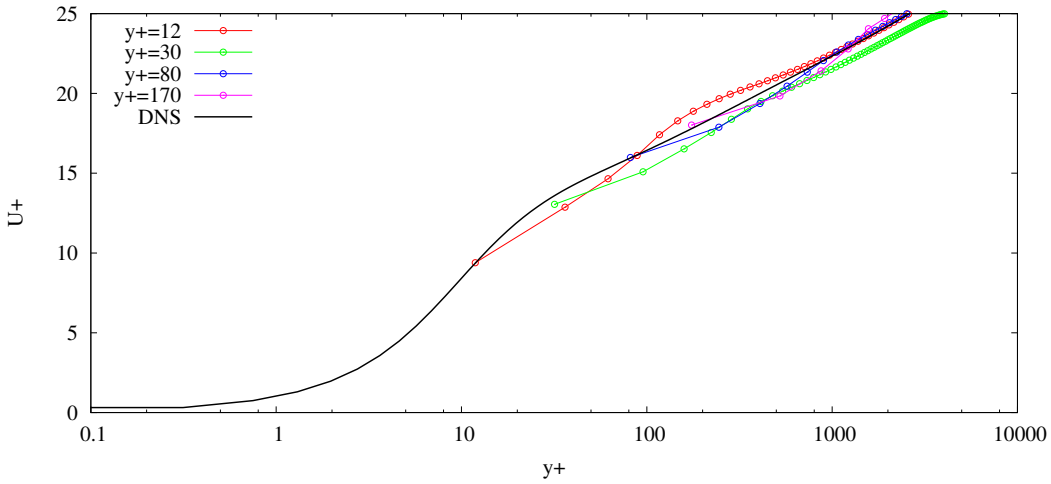

Figure 3.7: Channel flow at Re_τ=4,200 with IDDES and with a wall function

the flow being resolved with the large-eddy simulations. Approximately 99% of the finest grid is simulated with LES, 3% for the $y^+ \approx 30$ grid, 9% for the $y^+ \approx 80$ grid, and 17% for the coarsest $y^+ \approx 170$ grid. The typical RANS and LES regions are depicted in Figure 3.9. The results indicate that to have some predictive ability of the near-wall fluctuations with the IDDES approach, the first grid point off the wall needs to be placed before the end of the buffer region or below $y^+ = 30$. However, as the mean $U+$ profiles show, even smaller near-wall spacing is preferred. Coarse near-wall grids such as the $y^+ = 170$ grid are still capable of resolving the fluctuations away from the walls in the middle of the channel beyond $y^+ \approx 2000$.

4 Ahmed Body

The Ahmed body shown in Figure 4.1 is a simplified vehicle geometry originated by Ahmed et al. [1]. A series of wind tunnel experiments was performed to study the flow in the rear of the vehicle and the effects of the slant angle α on the vehicle's aerodynamic forces including lift and drag components. The body is 1044 mm long and it is mounted on four cylindrical stilts 50 mm above a fixed false floor that extends $1.35L$ upstream and $2.43L$ downstream. The wind speed is fixed at 60 m/s giving a length-based Reynolds number of $Re_L = 4.29 \times 10^6$. The Ahmed body has been studied extensively beyond the original work of Ahmed et al. [1] including the experimental and numerical studies of Gilliéron and Chometon [8], Lienhart et al. [16], Strachan et al. [26], Conan et al. [5], Joseph et al. [13], Thacker et al. [27], Serre et al. [20], among many others. The availability of a large dataset makes the Ahmed body an excellent validation case

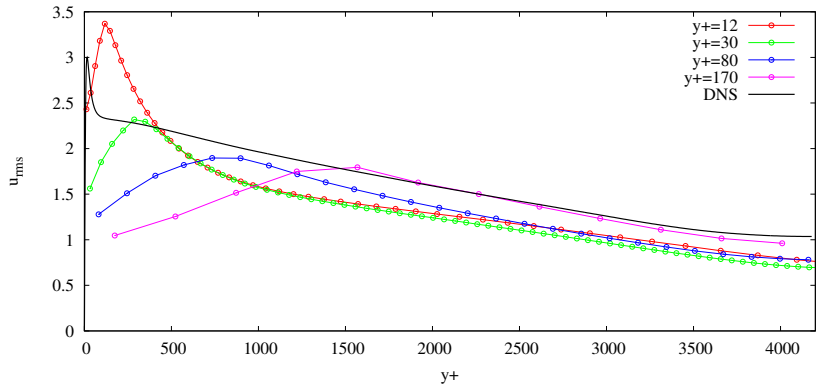

(a) RMS u velocity component

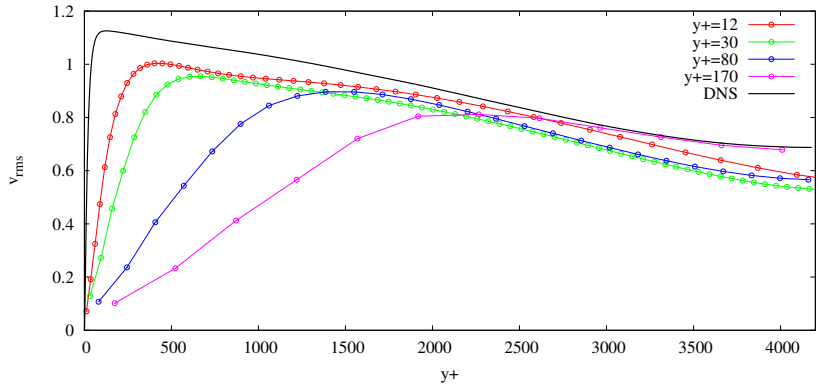

(b) RMS v velocity component

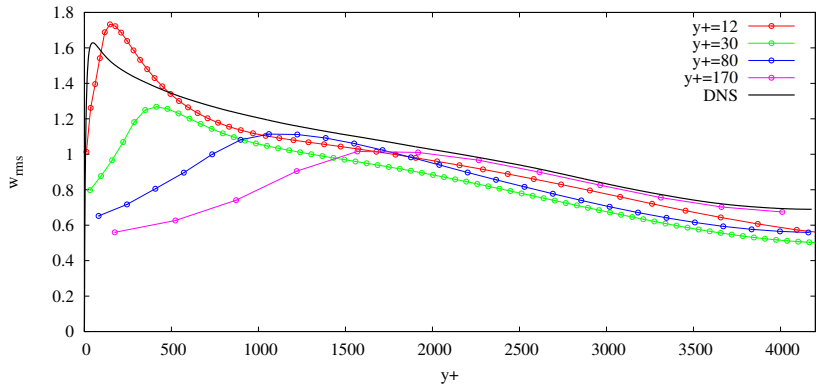

(c) RMS w velocity component

Figure 3.8: Channel flow at Re_τ=4,200 with IDDES and with a wall function

for numerical simulation techniques especially those pertaining to automotive and aerodynamic applications. The same geometry has been used in experimental and numerical investigations of various drag reduction techniques including static vortex generators, active air injection ports, and flaps [2, 9, 19].

Figure 3.9: Instantaneous snapshot of the RANS (blue) and LES (red) regions for the channel flow at Re_τ=4,200 with IDDES. Top row: $y^+ = 10$, $y^+ = 30$, bottom row: $y^+ = 80$, $y^+ = 170$

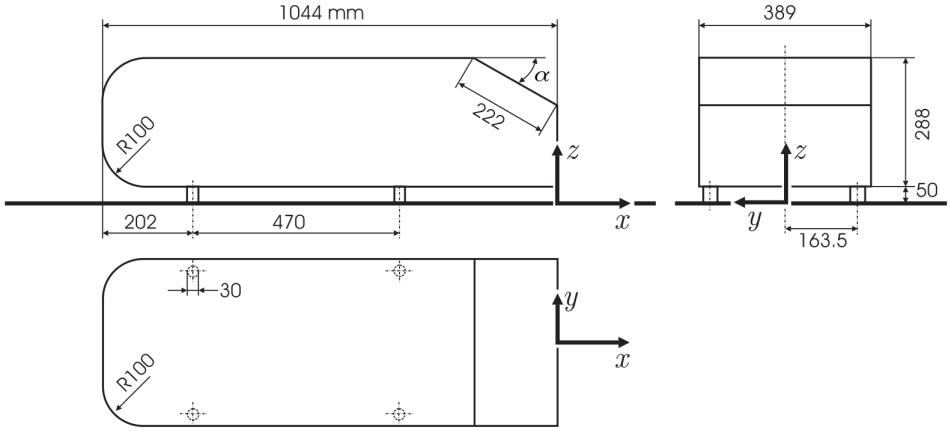

(a) Schematic view from Serre et al. [20]

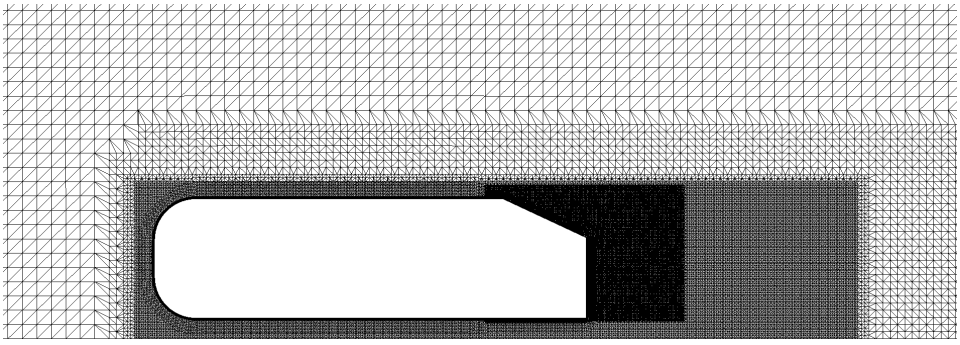

(b) Medium grid

Figure 4.1: Schematic view of the Ahmed body geometry and a close-up of the medium mesh sliced along the center-line. The slant angle α is equal to 25° and the support legs are not included in the numerical simulations.

Case	Cell Count (10^{-6})	Turb. Model	Average y^+	$\Delta tU/L$ (-)
DOEE-WR	30.2	DOEE	1	0.0001
DOEE-fine	21.1	DOEE	5	0.0002
DOEE-medium	7.91	DOEE	20	0.0005
DOEE-coarse	0.78	DOEE	40	0.0012
OEE-medium	7.91	OEE	20	0.0005
IDDES-WR	30.2	SA-IDDES	1	0.0001
IDDES-fine	21.1	SA-IDDES	5	0.0002
IDDES-medium	7.91	SA-IDDES	30	0.0003
IDDES-coarse	0.78	SA-IDDES	80	0.0013

Table 4.1: Summary of the Ahmed body simulation configurations. Wall-modeled cases use the universal Spalding wall function.

The slant angle of $\alpha = 25^\circ$ is selected for all simulations performed in this work. The length-based Reynolds number $Re = 1.39 \times 10^6$ is approximately three times smaller than in the experiments of Ahmed et al. [1]. The lower Reynolds number facilitates wall-resolved grids at a reduced computation effort. Furthermore, the drag coefficient of the Ahmed body is shown to be a relatively weak function of the Reynolds number [20]. Experimental measurements from the recent works of Thacker et al. [27] and Joseph et al. [13] conducted at the lower Reynolds number of 1.40×10^6 are also used in the evaluation of the present results. The wall-modeled DOEE and IDDES models are examined on a series of three grids and the wall-resolved equivalents are used on the finest grid. The three wall-modeled computational grids are generated with the semi-automatic tool snappyHexMesh whereas the finest wall-resolved grid is generated with the tool helyxHexMesh. The grid cell counts and the simulation parameters are summarized in Table 4.1. A centerline slice of the medium grid shown in Figure 1(b) illustrates the refinement regions used to resolve the wake and flow separation regions near the transition from the top to the slant surface. The second-order backwards scheme is selected for the temporal discretization and the stabilized linear-upwind scheme is used for the advection term to provide a balance between numerical stability and accuracy. The time-step size is automatically adjusted to limit the maximum Courant number to 0.9. The flow statistics are collected for five non-dimensional flow-overs after an initial transient start-up of two flow-overs.

The computational domain extends $2L$ upstream from the front of the vehicle and $4L$ downstream from the rear of the vehicle. The first section of the upstream floor is modeled as a slip boundary and thus the floor boundary layer does not begin to develop until $0.2L$ upstream of the vehicle nose where a no-slip wall is used. The domain is $2L$ wide and and L tall.

The following sections summarize the main findings of the numerical studies starting with a discussion on the salient features of the flow. The flow in the wake of the vehicle and flow separation are studied next by comparing a series of time-averaged and fluctuating velocity profiles to the experimental results of Lienhart et al. [16]. Then, the time-averaged drag coefficient as a function of grid refinement and turbulence model are compared to the experimental data. Finally, the computational effort required to complete the Ahmed body simulations is summarized to provide recommendations for industrial use of the OpenFOAM toolkit in high-Reynolds number external-flow applications.

4.1 Flow Structures

The flow structures around the Ahmed body are studied to understand the salient features that characterize this type of an external aerodynamic flow and to ensure a sufficient resolution of the flow features demonstrated through wind tunnel experiments (see Figure 4.2). Vortical structures are visualized through the Q-criterion defined as:

$$Q = \frac{1}{2}\left((\Omega)^2 - (S)^2\right) \tag{4.1}$$

where Ω is the vorticity tensor and S is the rate-of-strain tensor [12].

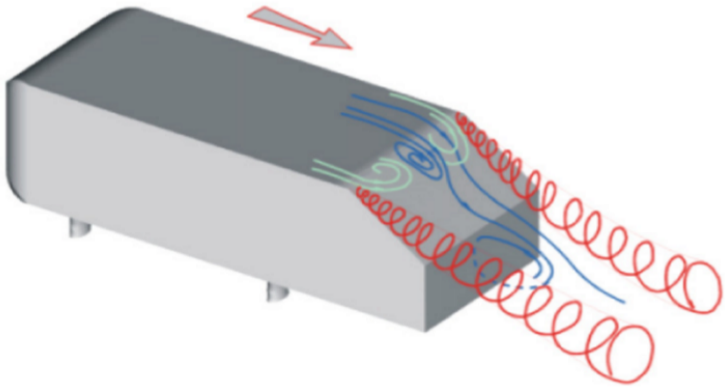

Figure 4.2: Sketch of the salient flow features around the Ahmed body with $\alpha = 25^\circ$ from Guilmineau [10]

4.1.1 Fine Wall-Function Grid

The top and profile views of the Ahmed body and contours of the Q-criterion on the fine wall-function grid are shown in Figure 4.3 for both the DOEE and ID-DES models. Near the front of the body around the transition from the nose to the bottom and side surfaces, both simulations resolve a pair of hairpin-like vorticies that stretch along approximately 75% of the body length. The top views illustrate

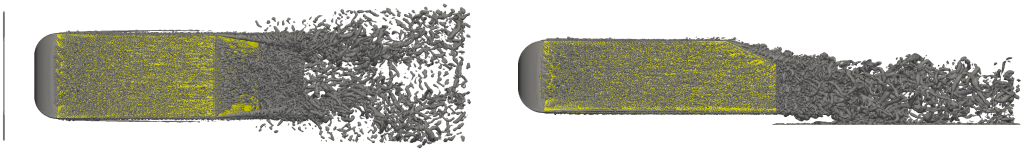

(a) DOEE

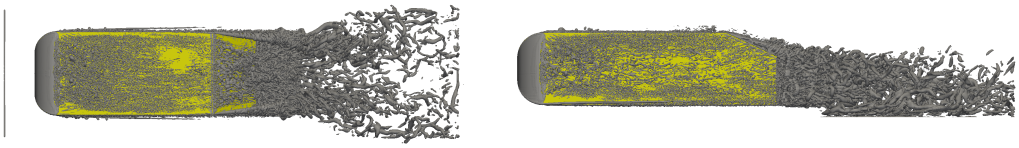

(b) IDDES

Figure 4.3: Flow structures (Q-criterion = 10^5) around the Ahmed body ($\alpha = 25°$) from the top (left) and side (right). Fine wall-function grid.

two strong counter-rotating vortices rolling off from the transition between the top and sides of the vehicle to the slant. These low-pressure inviscid structures compact the separated region along the slant surface and affect the pressure gradient in the wake of the body. An accurate resolution of these structures is necessary in predicting the reattachment of the boundary layer towards the lower section of the slant [20]. Both turbulence models yield similar distributions of the vortical structures in the rear region. The DOEE wake region has a slightly more dense concentration of vorticies but the salient features are well resolved in both simulations. The IDDES simulation resolves fewer small vortex filaments along the side and top surfaces within the attached boundary layer likely due to the damping effects of the RANS mode active in these areas.

4.1.2 Medium Wall-Function Grid

The medium grid iso-surfaces of the Q-criterion are depicted in Figure 4.4. The static one-equation eddy-viscosity model (OEE) is also used on the medium wall-function grid to investigate the benefits and limitations of the dynamic coefficient adjustment procedure for this problem. The dynamic model is shown to retain more of the small-scale vorticies along the top and side surfaces compared to the OEE and the IDDES simulations. Because the static OEE model coefficients are not adjusted based on the resolved information, the resulting effective viscosity is larger in the near-body region compared to the DOEE results leading to the suppression of the small vortical scales. The static model also retains the pair of front hairpin vorticies past the back plate of the Ahmed body and into the

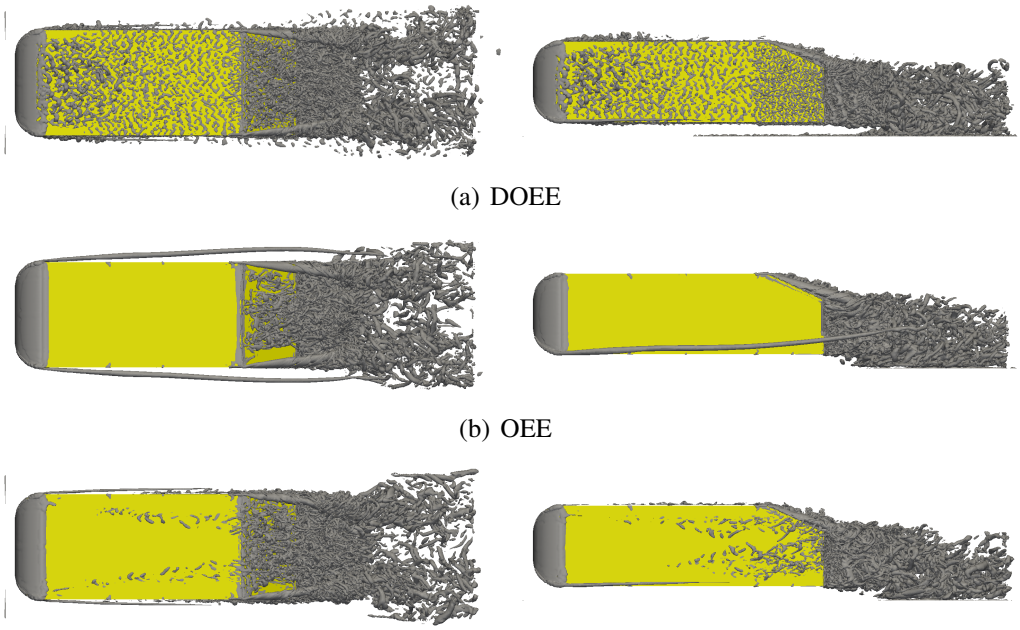

(a) DOEE

(b) OEE

(c) IDDES

Figure 4.4: Flow structures (Q-criterion = 10^5) around the Ahmed body ($\alpha = 25°$) from the top (left) and side (right). Medium wall-function grid.

turbulent wake. A survey of experimental results indicates that these structures break-down before reaching the rear of the vehicle and thus the results of the OEE model are likely an artifact of the turbulence model rather than of the flow physics. The OEE model dampens the small vortical structures in the slant region between the two counter-rotating vorticies and over predicts the length of the separation bubble along the centerline of the slant surface. Similar to the fine grid results, both DOEE and IDDES yield a similar distribution of flow features in the wake of the vehicle with DOEE retaining some of the smallest features. The large low pressure region in the rear is dominated by turbulent vortical structures without a particular directional alignment. The strong counter-rotating vorticies and the separation bubble in the slant region are resolved by both models.

4.1.3 Coarse Wall-Function Grid

The flow structures identified on the coarse grid with the same level of the Q-criterion are shown in Figure 4.5. The contour level is reduced by an order of magnitude in Figure 4.6 to identify some of the salient features that can be resolved on this relatively coarse grid. Both models resolve the small wake features and the counter-rotating vorticies to a lesser extent due to the grid resolution. The dynamic one-equation model is again found to retain a larger portion of the small-

est vortical structures, especially in the wake region and in the slant region. The IDDES model predicts a mostly attached boundary layer across the slant contrary to the experimental findings. The DOEE model is found to predict some separation in the upper part of the slant. Most small-scale vortical structures are not resolved on the coarse grid using the IDDES model because approximately 20% of the domain in the near-body region is simulated in the RANS mode. On the medium and fine grids where IDDES maintains the small scales only approximately 10% of the domain is active in the RANS mode. The RANS model in those cases is operating in the expected areas where the turbulent boundary layer remains attached.

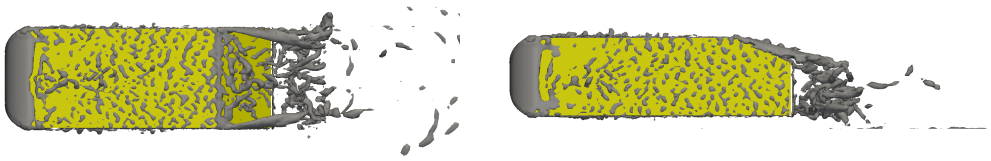

(a) DOEE

(b) IDDES

Figure 4.5: Flow structures (Q-criterion = 10^5) around the Ahmed body ($\alpha = 25^\circ$) from the top (left) and side (right). Coarse wall-function grid.

4.2 Wake Flow

The flow features in the rear of the vehicle are inspected further by studying time-averaged velocity streamlines and profiles as well as the fluctuating velocity profiles along the top and the slant surfaces. The numerical simulations performed here are compared against the experimental results of Lienhart et al. [16]. The main points of comparison in the time-averaged streamlines are the length and the characteristics of the recirculation regions behind the vehicle because the experimental streamlines are not captured in the near-body region. The velocity profiles along the top and the slant surfaces are used to examine this near-body region in greater detail to understand the ability of the present turbulence models in predicting flow separation and reattachment.

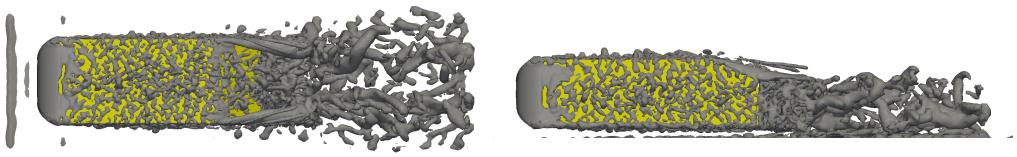

(a) DOEE

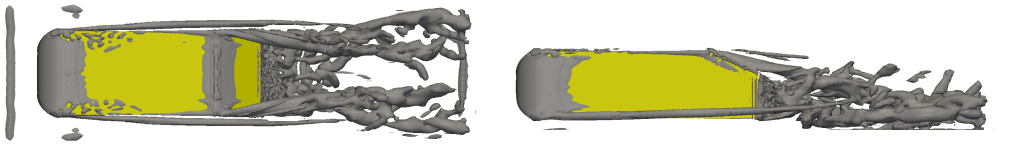

(b) IDDES

Figure 4.6: Flow structures (Q-criterion = 10^4) around the Ahmed body ($\alpha = 25°$) from the top (left) and side (right). Coarse wall-function grid.

4.2.1 Time-Averaged Wake Streamlines

The mean centerline streamlines calculated on the fine grid are shown in Figure 4.7. Both DOEE and IDDES predict a separation bubble at the transition edge between the top and the slant surfaces followed by reattachment of the flow near the midpoint of the slant. The sharp edge at the transition of the slant surface to the vertical back surface leads to a geometry-induced separation and the formation of a large recirculation region. Similarly, the ninety degree transition from the bottom surface to the back of the vehicle yields to the formation of a second smaller counter-rotating recirculation region. Both turbulence models predict a similar length of the recirculation zone of approximately 200 mm behind the back surface of the vehicle. The bottom region is larger in the DOEE results and hence the top recirculation region is compressed and reduced in size. Furthermore, the center of the top region is somewhat higher than what is reported in the experiments and somewhat lower in the IDDES results. In qualitative comparison, both models closely match the experimental results.

The medium grid results are summarized in Figure 4.8. The separation bubble at the top of the slant surface is captured by the DOEE and the IDDES simulations whereas the static OEE model significantly over predicts the size of the bubble. The recirculation zones in the rear are also poorly predicted with OEE compared to the results of DOEE and IDDES. The length of this zone is approximately 20% shorter than the experimental length and the top recirculation zone dominates the wake flow. A large separation bubble is also predicted on the no-slip floor near 100 mm $\leq x \leq$ 200 mm unlike in the other two simulations and the experimental measurements. The dynamic variant of the one-equation model yields a somewhat

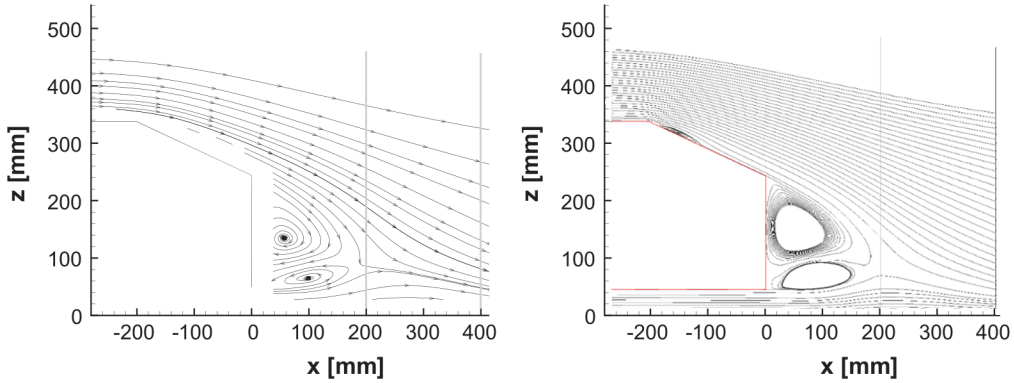

(a) DOEE

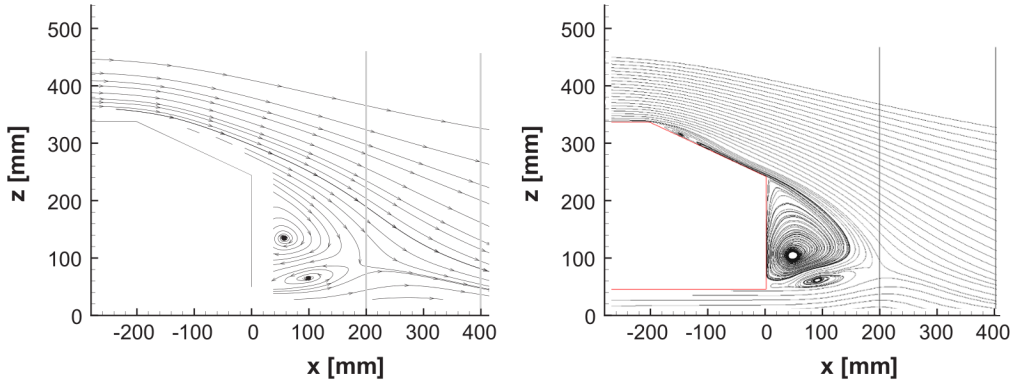

(b) IDDES

Figure 4.7: Time-averaged velocity streamlines in the wake for the fine wall-function grid compared to the experimental results of Lienhart et al. [16] (left column)

longer recirculation length than IDDES but both methods successfully predict the mean wake flow along the centerline.

Figure 4.9 presents the time-averaged streamlines computed on the coarse grid. The lack of the upper slant separation bubble in the IDDES simulation is the most striking result especially when compared to the DOEE results. The dynamic model is capable of capturing the separation bubble on a fairly coarse grid with less than one million cells whereas the IDDES method completely misses this important flow feature and the related adverse pressure gradient. Additionally, the IDDES simulation yields an unphysical separation bubble on the no-slip floor similar to what is predicted by the OEE model on the medium grid. The length of the recirculation regions is similar with both methods but the DOEE simulation better predicts the weakening of the top region and the mean trajectory of the streamlines.

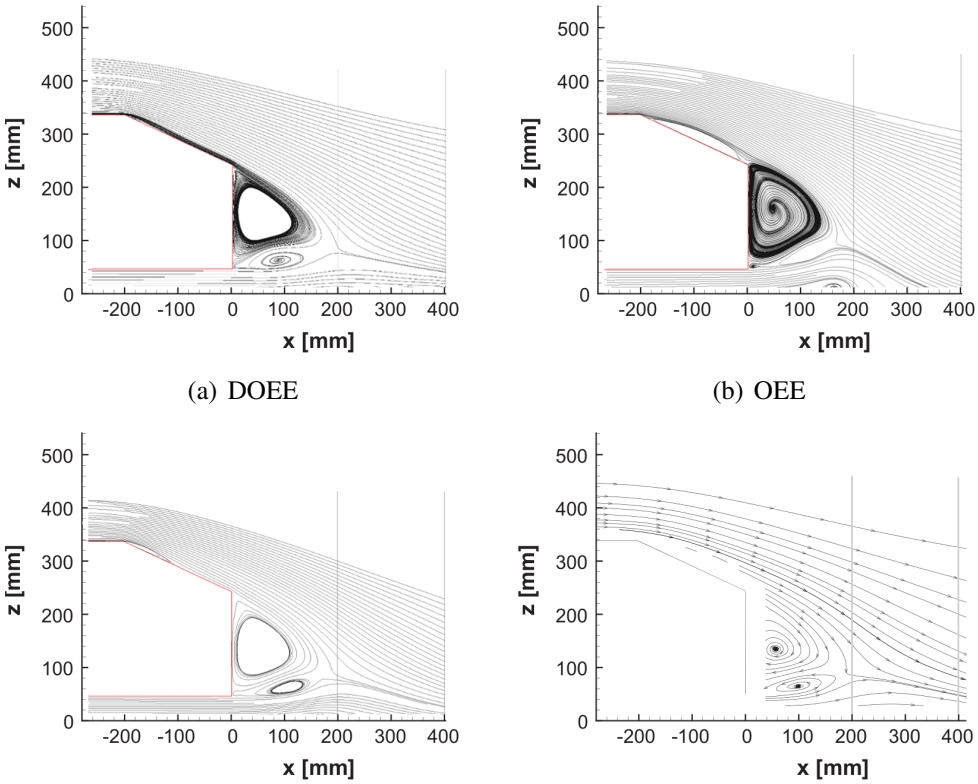

(a) DOEE (b) OEE

(c) IDDES (d) [16]

Figure 4.8: Time-averaged velocity streamlines in the wake for the medium wall-function grid

4.2.2 Velocity Profiles

The characteristics of the separation bubble near the upper section of the slant surface are examined by sampling the time-averaged and fluctuating velocity components along 13 vertical sample lines on the centerline of the vehicle. This detailed study allows for a direct comparison of the predictive capability of each turbulence model of the complex near-body flow.

The time-averaged streamwise velocity component is sampled on the fine wall-function grid and compared against the experimental data in Figure 4.11. The upper slant region including the end of the top surface compares well with the experiments using both turbulence modeling techniques. The flow remains attached until reaching the transition edge where flow separation is captured by both models with strong agreement to the experimental data. The flow reattaches at approximately $x = -100$ mm or the mid point of the slant and the lower section of the slant surface is characterized by an attached turbulent boundary layer. The IDDES simulation better predicts the reattachment and the resulting attached

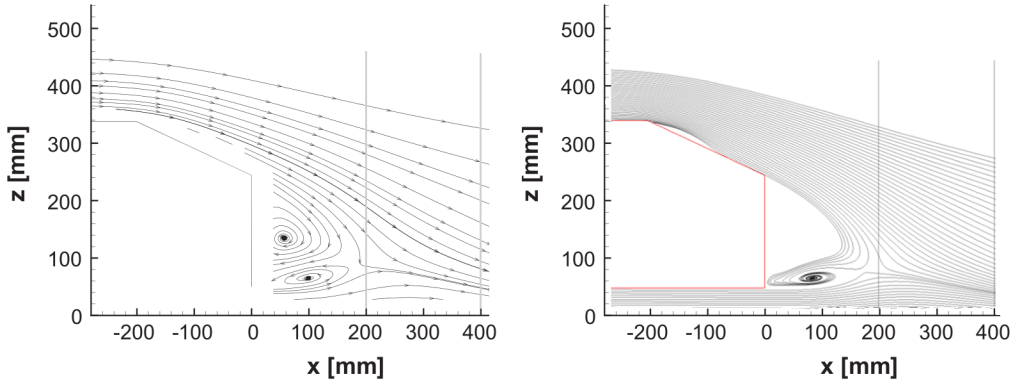

(a) DOEE

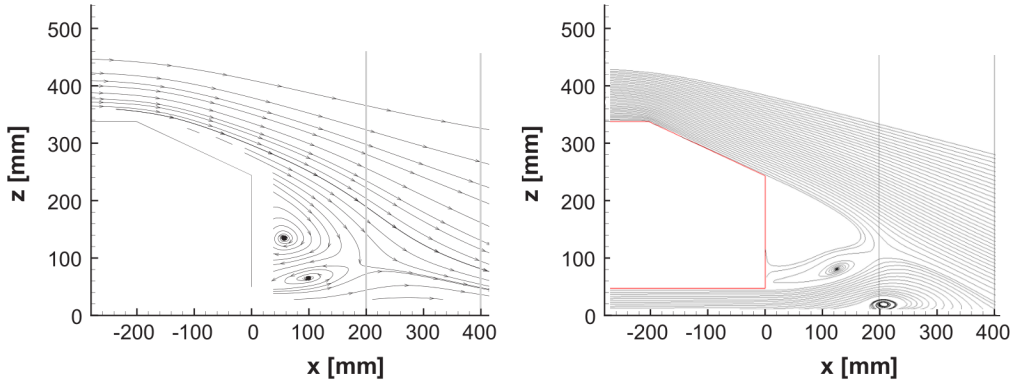

(b) IDDES

Figure 4.9: Time-averaged velocity streamlines in the wake for the coarse wall-function grid compared to the experimental results of Lienhart et al. [16] (left column)

boundary layer on the lower section of the slant. The DOEE simulation over predicts the magnitude of the streamwise velocity component and both methods somewhat over predict the mean velocity near the edge at $x = 0$ mm. The fluctuating streamwise velocity component is shown in Figure 4.12. The streamwise component dominates the spanwise and vertical components in this flow and thus it is an appropriate proxy for the resolved turbulent kinetic energy. The predicted profiles along the top and slant surfaces are very similar between the two models and both match the experimental results well. The near-body magnitude is somewhat under predicted between -160 mm $\leq x \leq -100$ mm where the flow is separated but once the flow reattaches both models predict the measured fluctuations.

The wall-resolved grid results are summarized in Figures 4.13 and 4.14. A finer resolution of the viscous sublayer with an average $y^+ = 1$ should improve the

overall prediction of the near-body flow characteristics. However, the mean flow in the separation bubble is under predicted and the reattachment point is lower along the length of the slant surface than in the fine wall-function grid results and the experiments. The fine near-wall resolution does improve the mean flow velocity towards the end of the vehicle. The fluctuating component is mostly under predicted within the separation bubble likely due to the over predicted length of this feature and thus an overall weakening of the flow inside.

The poorer results along the upper section of the slant can be explained by the collapse of the prism layers at the transition edge as shown in Figure 4.10. (*We note that we are novice users of helyxHexMesh, indeed this is the first time we have used the software to generate a grid. The tool has the intrinsic capability to generate continuous prism layers over the slant edge, it is just that within the time constraints of our work we were not able to go back and generate such a grid.*)

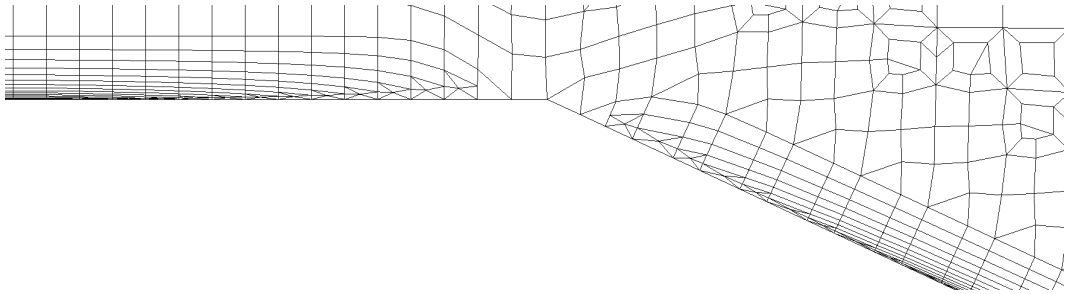

Figure 4.10: Collapse of near-body prism layers around the top-to-slant transition region on the wall-resolved grid

The relatively high Reynolds number requires extremely small near-body cells on the order of 10^{-5} m to produce a wall-resolved grid. These cells are generated along the length of most surfaces of the Ahmed body but their large aspect ratio results in the collapse of the prism layers near relatively sharp edges. The grid generation processes attempts to smoothly transition to where no prism layers can be grown but the extreme jump in cells size at this critical location is likely affecting the ability of the DOEE and IDDES models to correctly resolve the separation bubble. Additionally, the small cell size required to resolve the viscous sublayer increases the overall cell count by approximately 50% relative to the $y^+ = 5$ grid.

The results of the three turbulence models tested on the medium grid are summarized in Figures 4.15 and 4.16. Before separation on the top surface, the IDDES and OEE models under predict the mean velocity unlike the DOEE simulation. The vortical structures across the top surface identified in the previous discussion also indicate that the DOEE model is often capable of accurately describing the attached turbulent boundary layer. However, once the flow separates, the IDDES method is superior in predicting the mean and the turbulent near-body velocity

profiles. For example, Figures 4.15 and 4.16 show the streamwise time-averaged and the RMS velocity component on the lower slant section, respectively. The IDDES model closely matches the experimental data points whereas the OEE model significantly over predicts the size of the separation bubble – reaching all the way to the end of the vehicle – and the DOEE model under predicts the size of the separation bubble. On the medium grid, the IDDES simulation yields an average y^+ of approximately 30, right at the upper end of the buffer region. The high Reynolds number channel flow results show that this non-dimensional near-wall spacing is still capable of resolving the near-wall behavior but with larger y^+ values the RMS components are unlikely to be resolved accurately.

The coarse grid results shown in Figures 4.17 and 4.18 verify the channel flow findings. On this grid, the average y^+ using IDDES is approximately 80 and approximately 40 for the DOEE simulation. The mean flow within the attached boundary layer across the top surface is captured by both models but IDDES fails to the predict the turbulent content and the separation bubble completely. The wall-modeled LES simulation with the DOEE model is found to be surprisingly predictive on this coarse grid. The points of separation and reattachment are capture accurately and the turbulent content within the separation bubble and the reattached boundary layer closely matches the experiments.

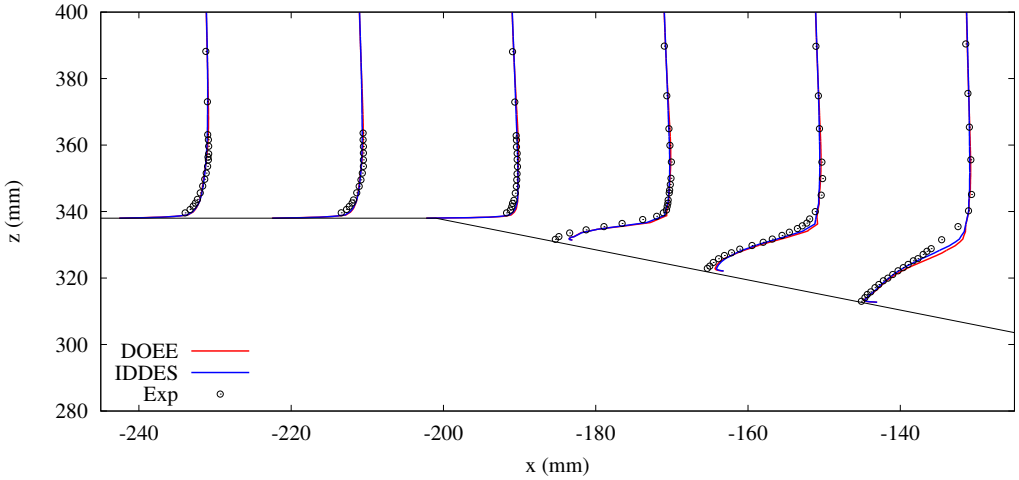

(a) Upper slant

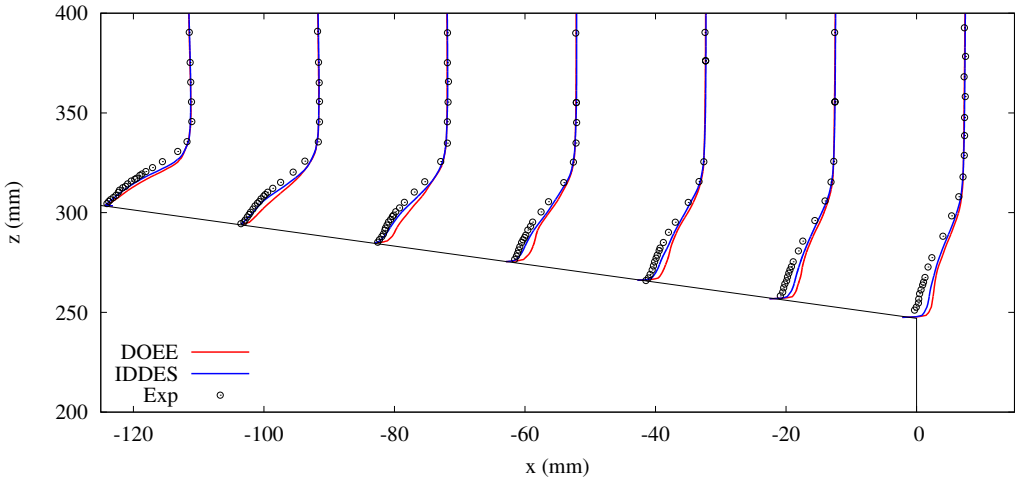

(b) Lower slant

Figure 4.11: Mean streamwise velocity profiles along the slant on the fine wall-function grid

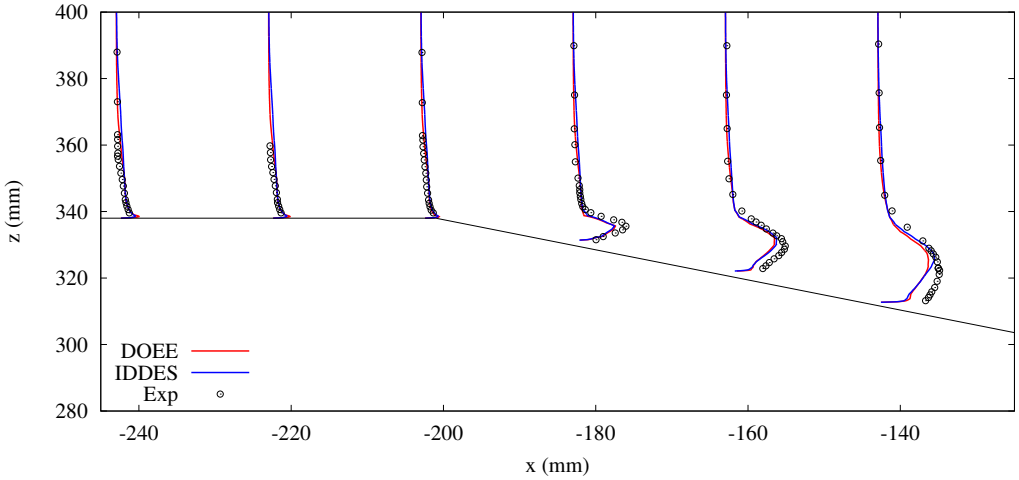

(a) Upper slant

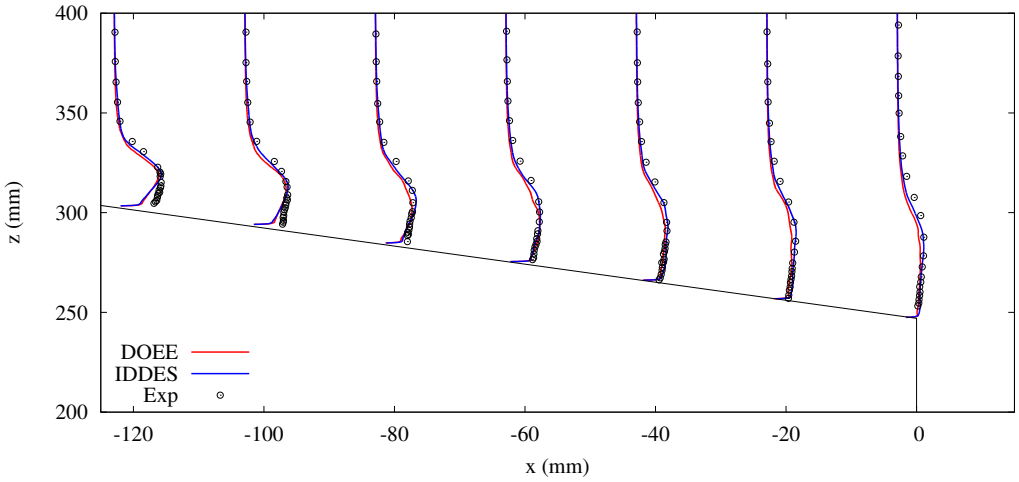

(b) Lower slant

Figure 4.12: RMS streamwise velocity profiles along the slant on the fine wall-function grid

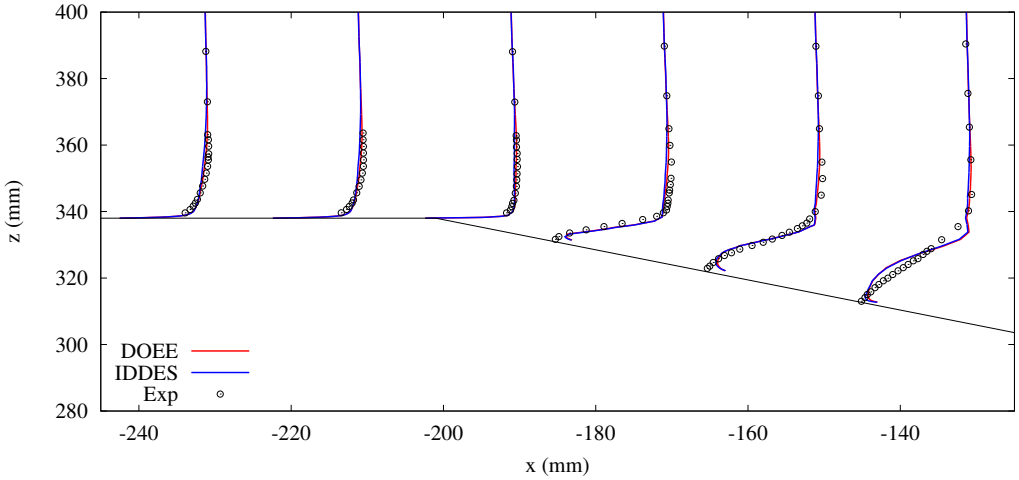

(a) Upper slant

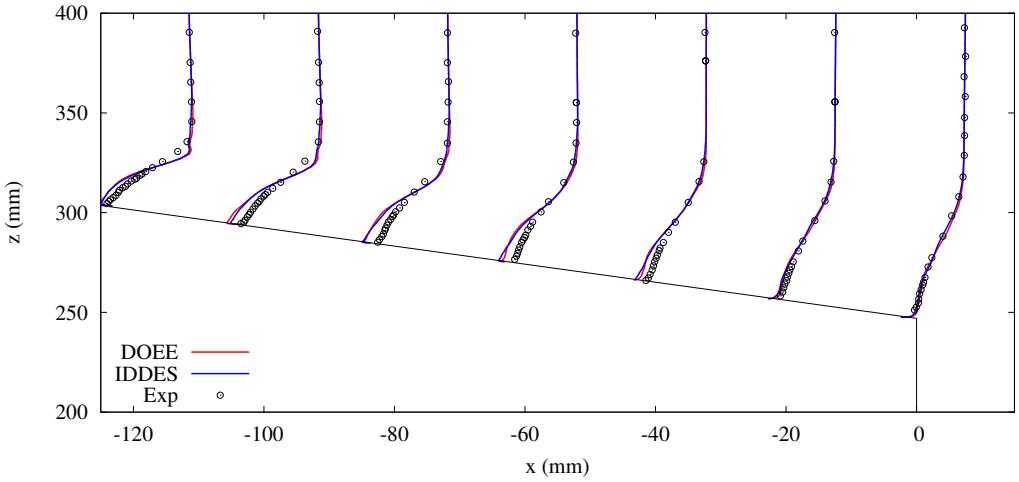

(b) Lower slant

Figure 4.13: Mean streamwise velocity profiles along the slant on the wall-resolved grid

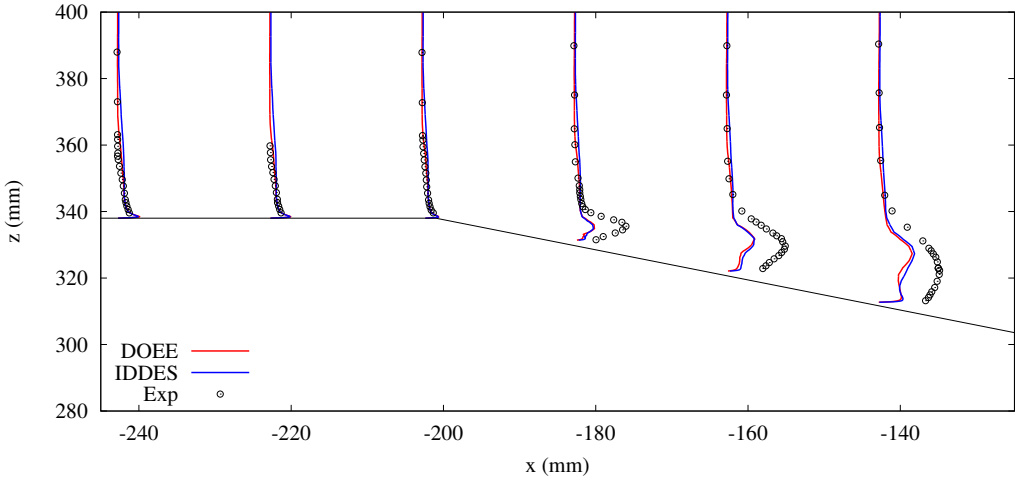

(a) Upper slant

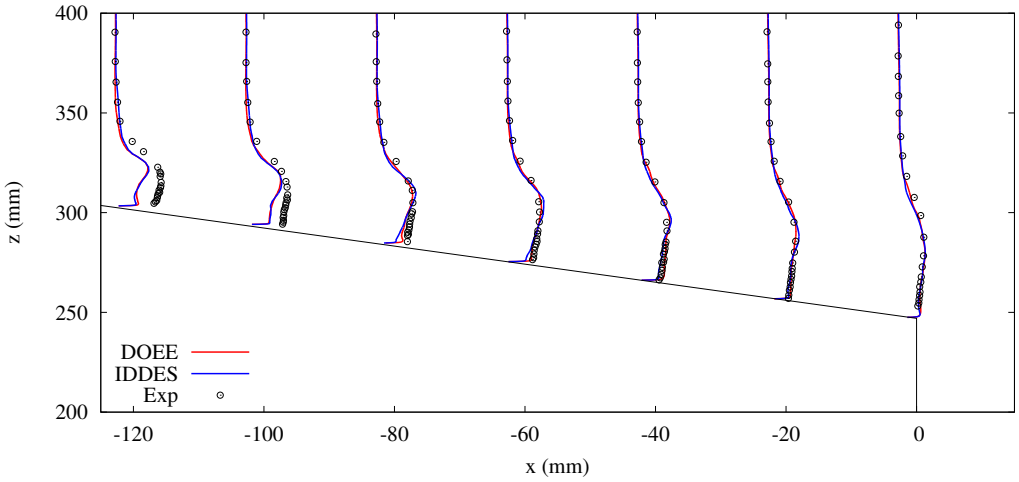

(b) Lower slant

Figure 4.14: RMS streamwise velocity profiles along the slant on the wall-resolved grid

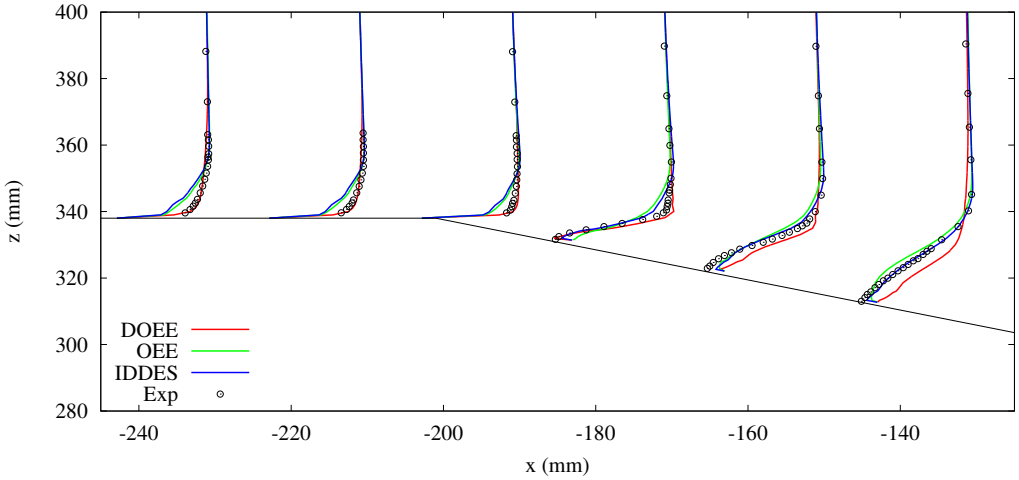

(a) Upper slant

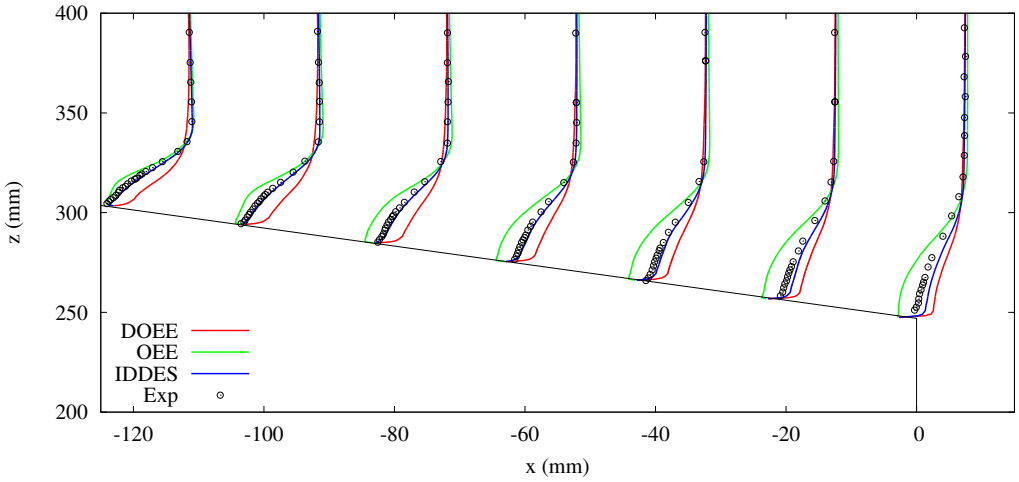

(b) Lower slant

Figure 4.15: Mean streamwise velocity profiles along the slant on the medium wall-function grid

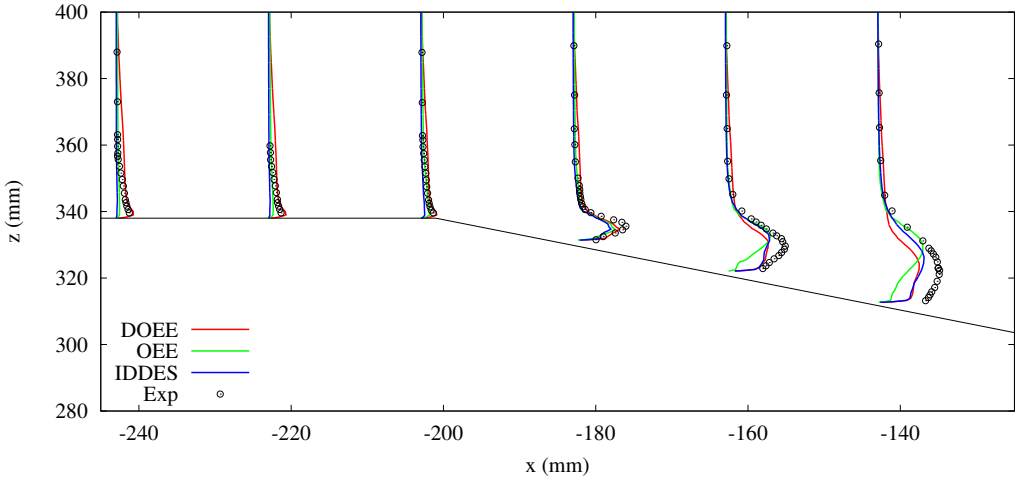

(a) Upper slant

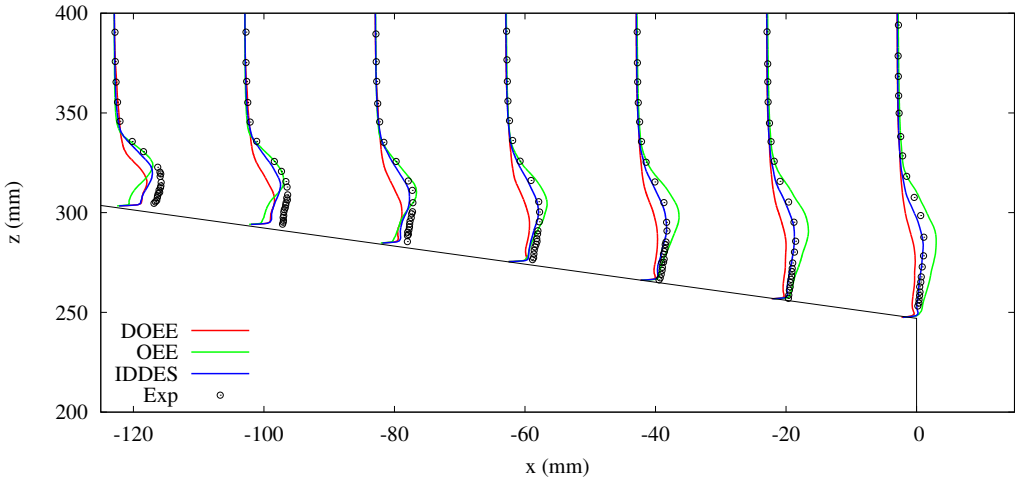

(b) Lower slant

Figure 4.16: RMS streamwise velocity profiles along the slant on the medium wall-function grid

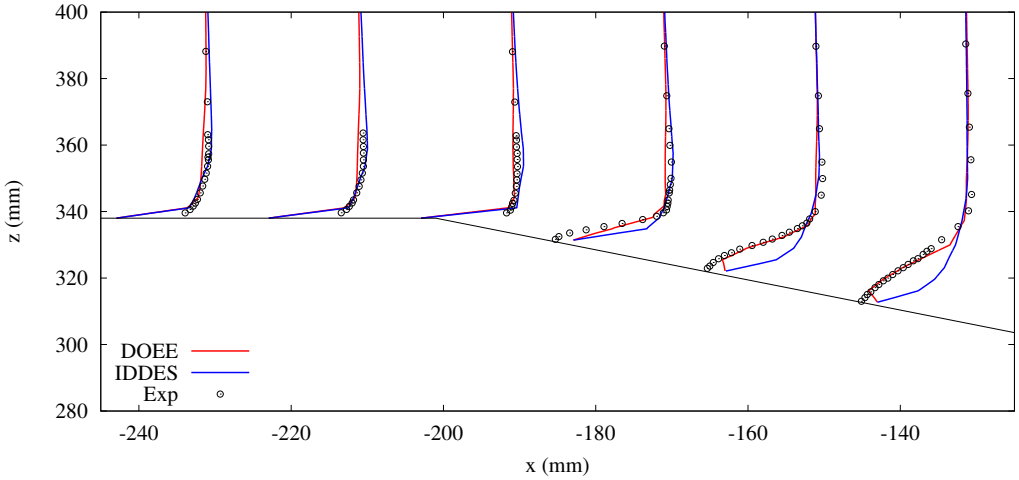

(a) Upper slant

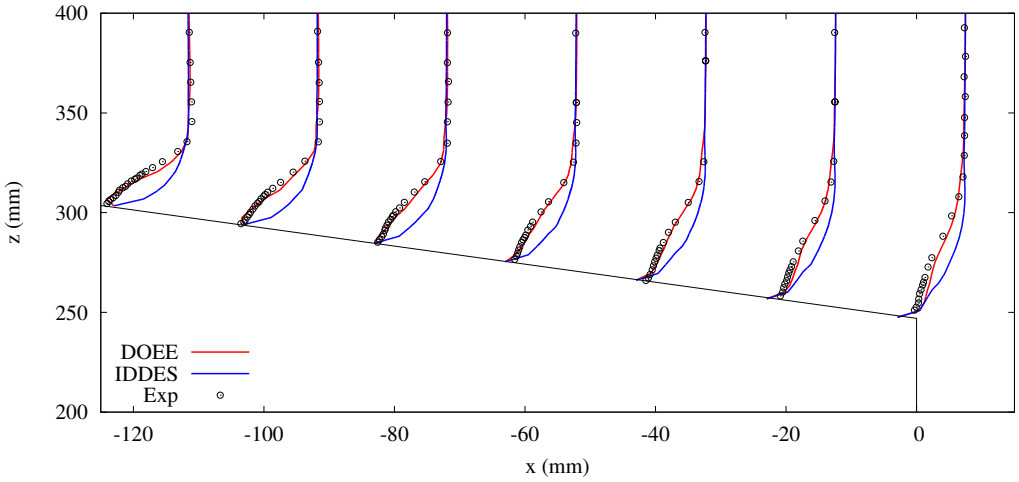

(b) Lower slant

Figure 4.17: Mean streamwise velocity profiles along the slant on the coarse wall-function grid

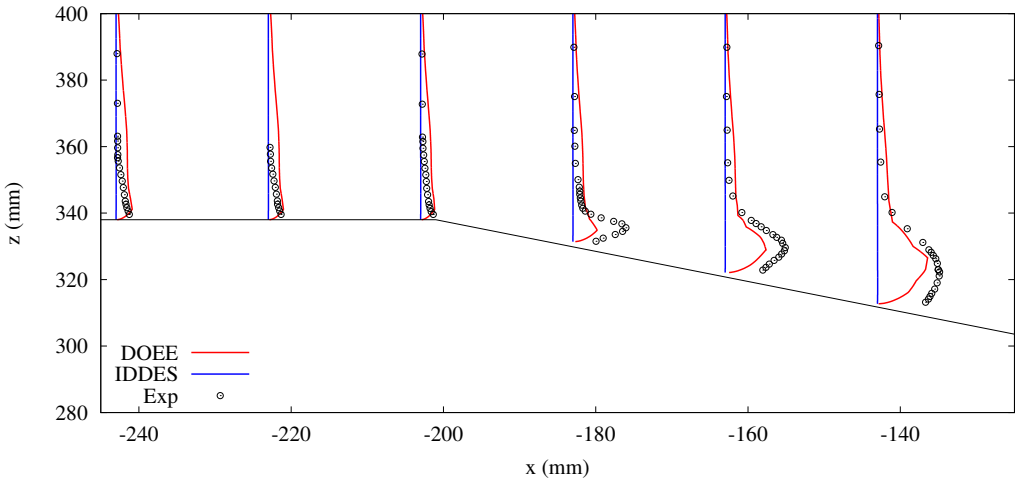

(a) Upper slant

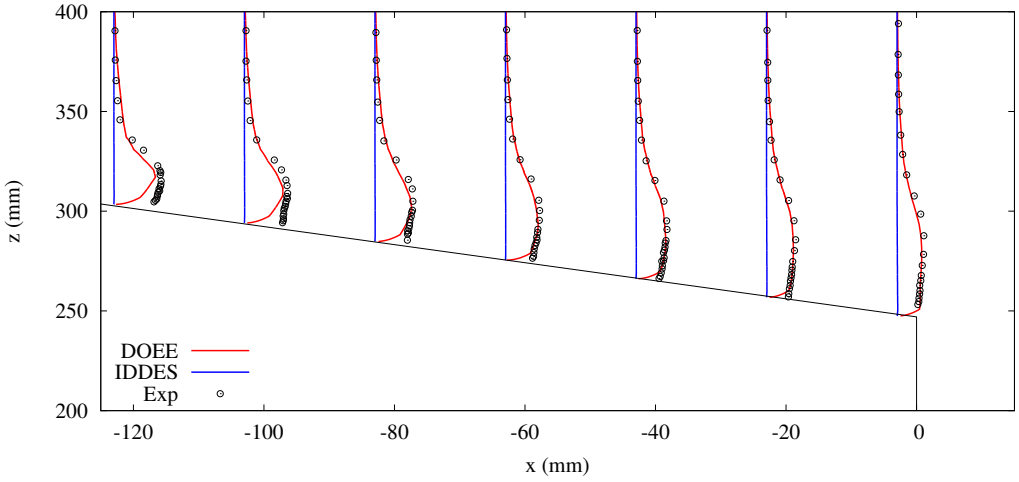

(b) Lower slant

Figure 4.18: RMS streamwise velocity profiles along the slant on the coarse wall-function grid

4.3 Aerodynamic Forces

An accurate prediction of the global flow quantities such as the drag coefficient is important to many industrial applications. Here, the time-averaged drag coefficient is computed as:

$$C_D = \frac{2F_x}{\rho U^2 A} \tag{4.2}$$

where F_x is the total force in the direction of the flow and the reference area A is the projected frontal area of the vehicle. The average drag coefficients as a

Case	Re (10^{-6})	C_D	Δ from [1] (%)	Δ from [27] (%)	Δ from [13] (%)
DOEE-WR	1.39	0.327	9.73	-9.17	7.21
DOEE-fine	1.39	0.306	2.68	-15.0	0.33
DOEE-medium	1.39	0.312	4.70	-13.3	2.30
DOEE-coarse	1.39	0.330	10.7	-8.33	8.20
OEE-medium	1.39	0.445	49.3	24.6	45.9
IDDES-WR	1.39	0.351	17.8	-2.50	15.1
IDDES-fine	1.39	0.337	13.1	-6.39	10.5
IDDES-medium	1.39	0.348	16.8	-3.33	14.1
IDDES-coarse	1.39	0.361	21.1	0.28	18.4
Ahmed et al. [1]	4.29	0.298	-	-17.2	-2.30
Thacker et al. [27]	1.40	0.360[1]	20.8	-	16.4
Joseph et al. [13]	1.40	0.305[1]	2.35	-14.1	-
Strachan et al. [26]	1.70	0.300[2]	0.67	-16.7	-1.64
Conan et al. [5]	3.48	0.313[1]	5.03	-13.1	2.62

Table 4.2: Drag coefficient as a function of grid refinement and turbulence modeling. Difference from the experimental value Δ is reported as a percentage.

function of grid refinement and turbulence modeling are summarized in Table 4.2. Several experimental studies with the slant angle of 25° are also summarized including the original work of Ahmed et al. [1], and more recent work by Thacker et al. [27], Joseph et al. [13], Strachan et al. [26], and Conan et al. [5]. The drag coefficients are corrected for the presence of the support legs and where necessary, an approximate support leg drag coefficient of $C_D^{legs} = 0.03$ is subtracted. The drag coefficients are also compared visually in Figure 19(a). The breakdown of the nose C_K, slant C_S, and back C_B surface pressure drag components is visualized against the experimental results of Ahmed et al. [1] in Figure 19(b). The residual viscous coefficient C_R is the difference between the total drag measured with load cells and the sum of the three pressure drag coefficients.

Both the IDDES and the DOEE series of simulations on the coarse, medium, and fine grids show a converging trend as a function of the grid refinement. The wall-resolved results depart from this trend due to the collapsed prism layers and thus a relatively poor prediction of the flow in the wake of the vehicle. The large C_D outlier result from the OEE simulation is expected because of the over predicted separation bubble and a poor estimation of the adverse pressure gradient. The series of DOEE simulations approach the experimental drag coefficient of Ahmed et al. [1] with a coefficient of 0.306 on the fine grid that is approximately 2.7% larger than the experimental measurement. This experimental drag coefficient is the lowest of many published results and it is contrasted by the recent results of Thacker et al. [27] who report a mean drag coefficient of 0.390 before correcting for the drag of the supports. The low drag coefficient reported by Ahmed et al. [1] may be related to the Reynolds number that is three times larger compared to the present study and the experiments of Thacker et al. [27] and

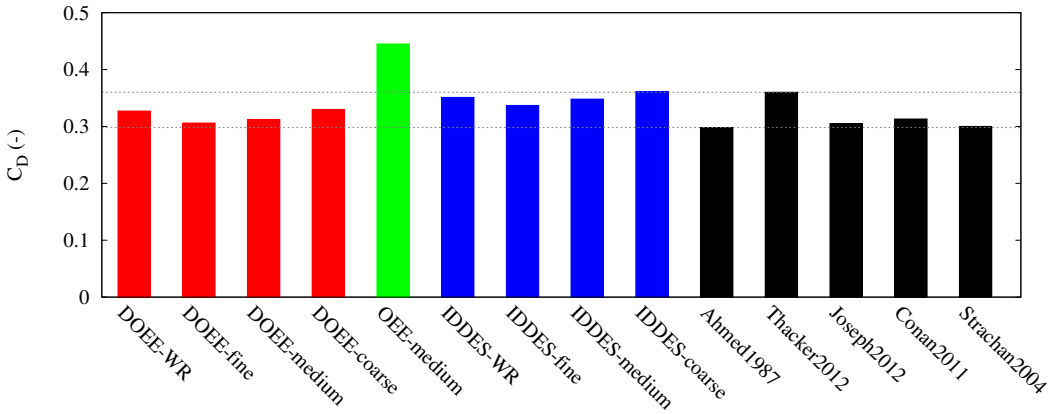

(a) Drag coefficient (experimental C_D corrected for support legs where necessary)

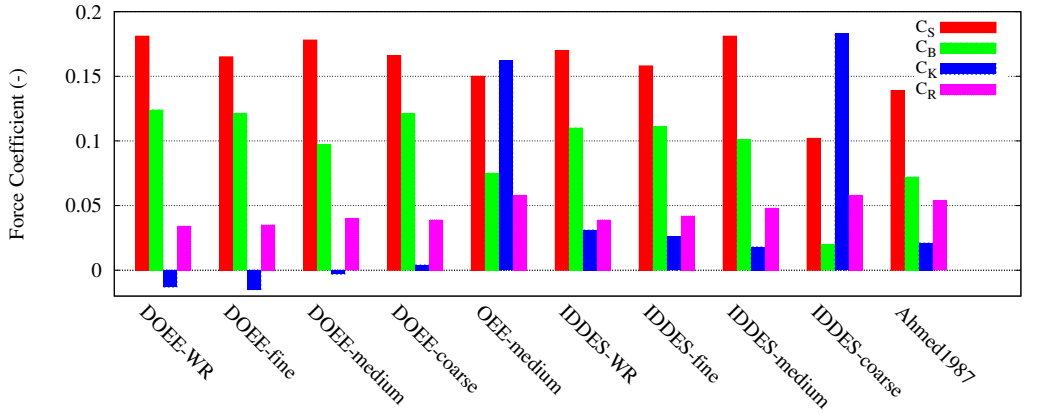

(b) Pressure drag (C_S, C_B, C_K) and viscous drag (C_R) components

Figure 4.19: Ahmed body ($\alpha = 25^\circ$) total drag coefficients and its components as a function of grid refinement and turbulence modeling

Joseph et al. [13]. A larger Reynolds number of $Re = 3.8 \times 10^6$ is also studied by Thacker et al. [27] and the reported drag coefficient $C_D = 0.384$ is approximately 1.6% smaller than at $Re = 1.4 \times 10^6$. The IDDES series of simulations convergences to a fine grid coefficient of 0.337 that is in-between the two extremes of the experimental results.

Pressure drag components and the residual viscous component are summarized in Figure 19(b). The simulations that fail to accurately describe the turbulent content across the slant surface and thus the separation of the flow (OEE and IDDES-coarse) are shown to significantly over predict the pressure drag of the nose surface. The separation bubble has a strong influence on the pressure distribution in the rear of the vehicle and thus on the pressure field around the entire body. The medium and fine IDDES results for the nose pressure drag are

close to the experimental value but both simulations over predict the back and slant pressure drag components and slightly under predict the viscous component. The DOEE simulations also over predict the back and slant components and under predict the viscous drag. Furthermore, the nose pressure drag is smaller than the experimental value and it becomes negative on the medium and fine grids. This net decrease in the pressure drag acts to reduce the total drag coefficient and to bring the numerical values closer to those of Ahmed et al. [1]. However, the cancellation of the pressure drag components does not correspond to the measured component breakdown. Overall, the fine IDDES simulation yields a pressure and viscous drag distribution that is the most similar to the experimental findings of Ahmed et al. [1].

4.4 Computational Effort

The computational effort for the Ahmed body simulations is summarized in Table 4.3. The FLUX High Performance Computing (HPC) cluster the University of Michigan is used to perform all simulations. The number of computational cores used for each case is varied as a function of the grid size to yield a maximum of approximately 50,000 cells per core. The execution times required to compute a single flow-over or the time for a particle to move from the front to the back of the Ahmed body are listed in wall-hours (physical time).

The fine grid results indicate that the one-equation model requires approximately 7% more computing time compared to the IDDES model. However, the opposite is found on the medium grid where the IDDES simulation takes approximately 8% more wall-hours. The overall computational cost is thus similar between DOEE and IDDES and the variation reported here is likely linked to the variability in the hardware used for each simulation[4]. The similarity in the execution time is expected because both models rely on a single transport equation, a wall function, and because of the consistency of the numerical method and of the grids used for benchmarking.

The timing results between the IDDES and the OEE simulation can be used as a proxy to demonstrate the scaling of the pimpleFoam solver as a function of the number of cores. The OEE simulation uses the medium grid and 120 more cores than the IDDES simulation using the same grid resolution. The turbulence modeling is different between these two cases but neither model uses a dynamic procedure to compute the subgrid stresses unlike the DOEE model. Furthermore, both IDDES and OEE models solve a single transport equation and both use a wall function. Between the 180 cores used for IDDES-medium and 300 cores

[1] Approximate drag of the support legs used in experiment ($C_D^{legs} = 0.03$) is subtracted

[2] Moving floor, no support legs

[3] Initialized from medium-grid results

[4] FLUX HPC is composed of over 16,000 cores that vary in hardware architecture and efficiency

Case	Cell Count (10^{-6})	Cores (-)	Memory (GB)	Time / Flow-Over (hr)
DOEE-WR^3	30.2	600	1,800	8.05
DOEE-fine^3	21.1	300	900	4.04
DOEE-medium	7.91	180	540	0.81
DOEE-coarse	0.78	60	180	0.06
OEE-medium	7.91	300	900	0.49
IDDES-WR^3	30.2	504	1,512	9.19
IDDES-fine^3	21.1	300	900	3.77
IDDES-medium	7.91	180	540	0.89
IDDES-coarse	0.78	48	144	0.14

Table 4.3: Summary of the computational effort for the Ahmed body simulations

for OEE-medium cases, the solver is shown to have close to a linear scaling in execution time.

5 Conclusions

This report summarizes two benchmarking studies focusing on the numerical simulation of high-Reynolds number external flows with applications to many industrial problems. The canonical flow of a fully-developed turbulent channel flow and the flow past the Ahmed body are evaluated using LES and hybrid RANS/LES models. Wall-resolved and wall-modeled large-eddy simulations using the one-equation eddy-viscosity and its dynamic variant are evaluated as well as the improved delayed detached-eddy simulations based on the one-equation Spalart-Allmaras model.

The channel flow problem is based on a relatively simple geometry of two parallel no-slip plates and a turbulent flow driven by a pressure gradient. Two Reynolds numbers are simulated to evaluate the sensitivity of the models to the size of the attached boundary layer and the resolution of the viscous sublayer. The universal wall-function of Spalding [25] is applied at both Reynolds numbers and it is found to have some sensitivity to the near-wall resolution as well as to the turbulence modeling approach. The IDDES model is more robust than the LES models across the range of Reynolds numbers and the non-dimensional distance to the wall of the first grid point. The resolution of the near-wall velocity fluctuations requires near-wall spacing of less than $y^+ \approx 15$. The fluctuations are shown to be damped by the RANS mode of IDDES when the first grid point off the wall is placed deeper into the buffer region or in the log layer.

The flow past the Ahmed body with the slant angle of $\alpha = 25^\circ$ is evaluated at the length-based Reynolds number of $Re = 1.39 \times 10^6$. Both the wall-modeled LES and IDDES methods are shown to accurately resolve the inviscid salient features of the flow including the counter-rotating vorticies shed at the transition point

between the top and the slant surfaces. The separation bubble formed at the top of the slant is captured on all grids using the dynamic one-equation eddy-viscosity LES model including a relatively coarse grid composed of approximately 780,000 cells. The IDDES method incorrectly predicts a fully-attached flow across the slant surface on the same coarse grid. However, the turbulent content within the separation bubble and the reattached boundary layer are predicted more accurately with IDDES on the medium and fine wall-function grids. The breakdown of the individual pressure drag components including the nose, slant, and back surfaces as well as the viscous component computed on the fine IDDES grid are found to be the closest to the experimental results of Ahmed et al. [1].

The robustness of the wall-modeled LES approach based on the dynamic one-equation eddy-viscosity model across a range of grid resolutions is an important feature for application to high-Reynolds number external flows. This approach is found to predict some of the most important features of a ground vehicle flow using relatively coarse grids that are useful in the early design stages. The IDDES approach is demonstrated to yield better predictions of the near-body flow including regions of attached and separated flow as long as a sufficiently fine grid is used. Furthermore, the IDDES model better predicts the individual drag components compared to the wall-modeled LES approach. The findings reported in this work demonstrate that both the hybrid RANS/LES methods and wall-modeled LES are viable options for external aerodynamic simulations.

Acknowledgments

The authors would like to acknowledge the Advanced Research Computing (ARC) center at the University of Michigan for providing support with the parallel computations.

References

[1] S. R. Ahmed, G. Ramm, and G. Faltin. Some salient features of the time-averaged ground vehicle wake. In *SAE Technical Paper Series*, 1984.

[2] Jean-François Beaudoin and Jean-Luc Aider. Drag and lift reduction of a 3D bluff body using flaps. *Experiments in Fluids*, 44:491–501, 2008.

[3] J. Bredberg. On the wall boundary condition for turbulence models. Technical report, Chalmers University of Technology, 2000.

[4] D. Carati, S. Ghosal, and P. Moin. On the representation of backscatter in dynamic localization models. *Physics of Fluids*, 7:606–616, 1995.

[5] B. Conan, J. Anthoine, and P. Planquart. Experimental aerodynamic study of a car-type bluff body. *Experimental Fluids*, 50:1273–1284, 2011.

[6] Jochen Fröhlich and Dominic von Terzi. Hybrid les/rans methods for the simulation of turbulent flows. *Progress in Aerospace Sciences*, 44:349–377, 2008.

[7] Massimo Germano, Ugo Pimoelli, Parviz Moin, and William H. Cabot. A dynamic subgrid-scale eddy viscosity model. *Physics of Fluids*, 3:1760–1765, 1991.

[8] Patrick Gilliéron and Francis Chometon. Modelling of stationary three-dimensional separated air flows around an ahmed reference model. In *ESAIM: Proceedings*, 1999.

[9] Patrick Gilliéron and Azeddine Kourta. Aerodynamic drag reduction by vertical splitter plates. *Experiments in Fluids*, 48:1–16, 2010.

[10] Emmanuel Guilmineau. Computational study of flow around a simplified car body. *Journal of Wind Engineering and Industrial Aerodynamics*, 96: 1207–1217, 2008.

[11] Jessica Gullbrand and Fontini Katopodes Chow. The effect of numerical errors and turbulence models in large-eddy simulations of channel flow, with and without explicit filtering. *Journal of Fluid Mechanics*, 495:323–341, 2003.

[12] George Haller. An objective definition of a vortex. *Journal of Fluid Mechanics*, 525:1–26, 2005.

[13] Pierre Joseph, Xavier Amandolese, and Jean-Luc Aider. Drag reduction on the 25° slant angle ahmed reference body using pulsed jets. *Experiments in Fluids*, 52:1169–1185, 2012.

[14] John Kim, Parviz Moin, and Robert Moser. Turbulence statistics in fully developed channel flow at low reynolds number. *Journal of Fluid Mechanics*, 177:133–166, 1987.

[15] Won-Wook Kim and Suresh Menon. A new dynamic one-equation subgrid-scale model for large eddy simulations. In *AIAA, Aerospace Sciences Meeting and Exhibit, 33 rd, Reno, NV*, 1995.

[16] H Lienhart, C Stoots, and S Becker. Flow and turbulence structures in the wake of a simplified car model (ahmed modell). In *New Results in Numerical and Experimental Fluid Mechanics III*. Springer, 2002.

[17] Adrián Lozano-Durán and Javier Jiménez. Effect of the computational domain on direct simulations of turbulent channels up to $Re_\tau = 4200$. *Physics of Fluids*, 26:011702, 2014.

[18] Stephen B. Pope. Ten questions concerning the large-eddy simulation of turbulent flows. *New Journal of Physics*, 6:1–24, 2004.

[19] G. Pujals, S. Depardon, and C. Cossu. Drag reduction of a 3d bluff body using coherent streamwise streaks. *Experiments in Fluids*, 49:1085–1094, 2010.

[20] Eric Serre, Matthieu Minguez, Richard Pasquetti, Emmanuel Guilmineau, Gan Bo Deng, Michael Kornhaas, Michael Schaefer, Jochen Froehlich, Christof Hinterberger, and Wolfgang Rodi. On simulating the turbulent flow around the ahmed body: A French–German collaborative evaluation of LES and DES. *Computers and Fluids*, 78:10–23, 2013.

[21] Mikhail L. Shur, Philippe R. Spalart, Mikhail Kh. Strelets, and Andrey K. Travin. A hybrid RANS-LES approach with delayed-DES and wall-modelled LES capabilities. *International Journal of Heats and Fluid Flow*, 29:1638–1649, 2008.

[22] P. Spalart. Detached-eddy simulation. *Annual Review Fluid Mechanics*, 41: 181–202, 2009.

[23] P. R. Spalart and S. R. Allmaras. A one-equation turbulence model for aerodynamic flows. *La Recherche Aerospatiale*, 1:5–21, 1994.

[24] PR Spalart, WH Jou, M Strelets, and SR Allmaras. Comments on the feasibility of les for wings, and on a hybrid rans/les approach. *Advances in DNS/LES*, 1:4–8, 1997.

[25] D. B. Spalding. A single formula for the "law of the wall". *Journal of Applied Mechanics*, 28:455–459, 1961.

[26] R. K. Strachan, K. Knowles, and N. J. Lawson. A cfd and experimental study of an ahmed reference model. In *SAE Word Congress Detroit, Michigan*, 2004.

[27] A. Thacker, S. Aubrun, A. Leroy, and P. Devinant. Effects of suppressing the 3d separation on the rear slant on the flow structures around an ahmed body. *Journal of Wind Engineering and Industrial Aerodynamics*, 107:237–243, 2012.

[28] Olivier Verhoeven. Trailing edge noise simulations. Master's thesis, Delft University of Technology, 2011.

[29] Akira Yoshizawa and Kiyosi Horiuti. A statistically-derived subgrid-scale kinetic energy model for the large-eddy simulation of turbulent flows. *Journal of the Physical Society of Japan*, 54:2834–2839, 1985.